

Shear banding in time-dependent flows of polymers and wormlike micelles

R. L. Moorcroft¹ and S. M. Fielding¹

Department of Physics, Durham University, Science Laboratories, South Road, Durham, DH1 3LE, UK

(Dated: 16 November 2021)

We study theoretically the formation of shear bands in time-dependent flows of polymeric and wormlike micellar surfactant fluids, focussing on the protocols of step shear stress, step shear strain (or in practice a rapid strain ramp), and shear startup, which are commonly studied experimentally. For each protocol we perform a linear stability analysis to provide a fluid-universal criterion for the onset of shear banding, following our recent Letter⁶¹. In each case this criterion depends only on the shape of the experimentally measured rheological response function for that protocol, independent of the constitutive properties of the material in question. (Therefore our criteria in fact concern all complex fluids and not just the polymeric ones of interest here. A separate manuscript³⁰ will explore them in a broad class of disordered soft glassy materials including foams, dense emulsions, dense colloids, and microgel bead suspensions.) An important prediction is that pronounced banding can arise transiently in each of these protocols, even in fluids for which the underlying constitutive curve of stress as a function of strain-rate is monotonic and a steadily flowing state is accordingly unbanded. For each protocol we provide numerical results in the rolie-poly and Giesekus models that support our predictions. We comment on the ability of the rolie-poly model to capture the observed experimental phenomenology, and on the failure of the Giesekus model.

I. INTRODUCTION

Many complex fluids show shear banding, in which an initially homogeneous shear flow undergoes an instability leading to the formation of macroscopic bands of differing viscosity, which coexist at a common shear stress^{29,55,62,68}. Examples include entangled polymer solutions and melts^{14,15,75,84}, triblock copolymer solutions^{11,56}, wormlike micellar surfactant solutions^{12,36,37,40,48,52–54,59,79}, lyotropic lamellar surfactant phases⁸⁰, concentrated suspensions and emulsions^{21,69}, carbopol microgels²⁴, star polymers⁷⁷ and foams⁷⁶.

To date, most studies have focused on the long-time rheological response of these fluids, once a steady flowing state has been established. The criterion for shear banding in this steady state limit is well known⁸⁹: that there exists a region of negative slope in the constitutive curve of shear stress as a function of shear rate for an underlying base state of stationary homogeneous flow. The steady state flow curve relation between stress and strain rate then exhibits a characteristic plateau in the shear banding regime, signifying a coexistence of bands of differing shear rates $\dot{\gamma}_l, \dot{\gamma}_h$ at a common value Σ_p of the shear stress. See Fig. 1.

However most practical flows involve a strong time-dependence, whether perpetually or during the initial startup of deformation before a steadily flowing state has been established. Accordingly, increasing experimental attention is now being devoted to time-dependent flow protocols. Shear banding has recently been reported following the imposition of a step stress^{12,15,22,32,38–41,83}, following a step shear strain^{9,12,13,28,49,72,88}, and during shear startup^{15,23,24,41,75}.

In each case the onset of banding appears closely linked to the presence of a distinctive signature in the shape of

the material's time-dependent rheological response function. Importantly, although this signature is specific to the particular flow protocol in question, it appears largely universal for all complex fluids in a given protocol. For example the onset of shear banding in the shear startup protocol appears closely related to the presence of an overshoot in the stress startup signal, as we shall elaborate below.

Motivated by these observations, in a recent Letter⁶¹ we derived fluid-universal criteria for the onset of linear instability to the formation shear bands, one for each protocol in turn: step stress, shear startup, and step strain. Each criterion depends only on the shape of the experimentally measured rheological response function for that protocol, *independent* of the mesostructure and constitutive dynamics of the particular material in question. These predictions for banding in time-dependent flows thus have the same highly general, fluid-universal status as the widely known criterion for banding in steady state (of a negatively sloping constitutive curve).

Whether or not the time-dependent shear bands predicted here persist to steady state of course depends on the shape of that underlying constitutive curve for stationary homogeneous flow. However an important contribution of this work is to highlight that pronounced banding often arises during a fluid's transient evolution to a steady flowing state, given the time-dependent flow signatures that we shall discuss, even in fluids for which the underlying constitutive curve is monotonic and the eventual steady state unbanded.

The present manuscript provides an in-depth discussion of the criteria outlined in Ref.⁶¹, and a thorough numerical exploration of them within two of the most popular models for the rheology of entangled polymeric fluids: the rolie-poly (RP) model and the Giesekus model. Accordingly, it addresses conventional polymeric fluids such as concentrated polymer solutions or melts of high

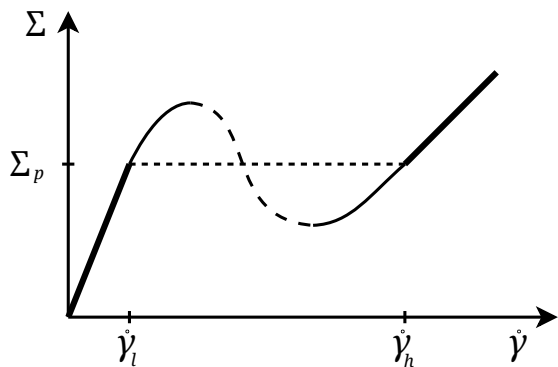


FIG. 1. Thin line: constitutive curve for an underlying base state of homogeneous shear flow. Homogeneous flow is linearly unstable in the dashed region. Thick lines joined by dotted plateau: corresponding steady state flow curve. For imposed shear rates in the plateau region $\dot{\gamma}_l < \dot{\gamma} < \dot{\gamma}_h$ the steady state is shear banded: see Fig. 2.

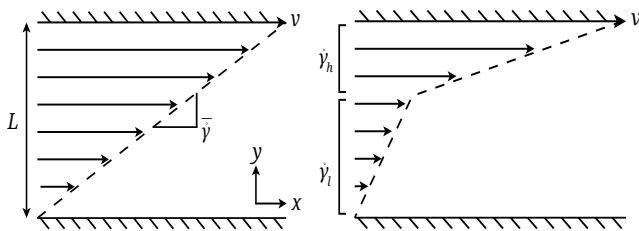


FIG. 2. **Left:** homogeneous flow profile. **Right:** shear banded flow profile.

molecular weight; as well as entangled wormlike micelles whose long, chain-like substructures undergo the same stress relaxation mechanisms as polymers, with the additional mechanisms of chain breakage and reformation²⁰. For convenience we refer to all these materials simply as ‘polymeric fluids’ in what follows. The reader is referred to a separate manuscript³⁰ for a discussion of the same phenomena in the context of a broad class of disordered soft glassy materials such as foams, dense emulsions, onion surfactants and microgel bead suspensions.

The paper is structured as follows. In section II we survey the experimental and simulation evidence for shear banding in time-dependent flow protocols. In Sec. III we outline a general theoretical framework for the rheology of complex fluids, and give details of the rolie-poly and Giesekus constitutive models of polymeric flows. In Sec. IV we detail a linear stability analysis for the onset of shear banding in time-dependent flows, performed within this general framework. In Secs. V, VI and VII we present our analytical criteria for the onset of shear banding in step stress, strain ramp, and shear startup protocols respectively, and give supporting numerical evidence in each case. We also discuss the way our predictions relate to experimental data. Conclusions and perspectives for further study are given in Sec. VIII.

Throughout the manuscript we use the term ‘constitu-

tive curve’ to describe the relation between shear stress and strain rate for an underlying base state of homogeneous shear flow. We use the term ‘flow curve’ to describe the relation between shear stress and applied strain rate $\bar{\dot{\gamma}}$ (averaged across the sample) for a steady flowing state. In any regime of homogeneous steady state flow, these two curves coincide.

II. EXPERIMENTAL AND NUMERICAL MOTIVATION

A. Step stress

Steady state shear banding is associated with a region of negative slope in the underlying constitutive curve of shear stress Σ as a function of shear rate $\dot{\gamma}$ for an underlying base state of stationary (though not necessarily stable) homogeneous flow. The composite flow curve $\Sigma(\dot{\gamma})$ for the steady state banded flow then typically displays a flat (or slightly upwardly sloping) plateau spanning a window of shear rates $\dot{\gamma}_l < \dot{\gamma} < \dot{\gamma}_h$ at (or spanning a small window about) a selected value of the stress Σ_p . See Fig. 1. Accordingly, steady state banding is relatively easily accessed in an applied shear rate protocol for imposed rates $\dot{\gamma}_l < \dot{\gamma} < \dot{\gamma}_h$, but much more difficult to access under conditions of a constant imposed stress, which must be tuned to lie in the small window of stress consistent with this near-plateau in the flow curve.

Nonetheless, following the imposition to a previously unloaded sample of a step stress in the vicinity of this plateau $\Sigma \sim \Sigma_p$, entangled polymeric materials commonly exhibit time-dependent shear banding^{12,14,15,38–41,83}. Its onset appears closely associated with a sudden and dramatic increase in the shear rate response of the system by several orders of magnitude over a short time interval, as it rises from a small initial value to attain its final value on the steady state flow curve^{12,14,39,40,73,83}. In some cases a return to homogeneous shear is seen as steady state is neared¹⁵, though this is often complicated by the occurrence of edge fracture, which can severely limit the determination of true steady state^{42,73}. Whether polymeric fluids exhibit steady state banding in the step stress protocol therefore remains an open question.

B. Strain ramp

In a strain ramp protocol, shear is applied at a constant rate $\dot{\gamma}_0$ for a time t^* until some desired strain amplitude $\gamma_0 = \dot{\gamma}_0 t^*$ is attained, after which the shearing is stopped. The limit $t^* \rightarrow 0$ and $\dot{\gamma}_0 \rightarrow \infty$ at fixed γ_0 gives a theoretically idealized step strain. Indeed in practice a rapid ramp is often termed a step strain.

The shear stress relaxation function $\Sigma(t')$ as a function of the time $t' = t - t^*$ elapsed since the end of the ramp is usually reported after scaling by the strain amplitude to give $G(t', \gamma_0) = \Sigma(t', \gamma_0)/\gamma_0$, with $G(t') =$

$\lim_{\gamma_0 \rightarrow 0} G(t', \gamma_0)$ in the small strain limit of linear response.

This protocol has been extensively studied experimentally in entangled polymeric fluids^{26,27,46,64–67,78,81,85}. The stress relaxation function typically shows a double exponential form, with time-strain separability characterised by the so-called “damping function” h for times greater than some $t' = \tau_k$:

$$h(\gamma_0) = \frac{G(t', \gamma_0)}{G(t')} \quad \text{for } t' \gg \tau_k. \quad (1)$$

Experimental data for this damping function in entangled polymers has been compared extensively with the form predicted theoretically by Doi and Edwards (DE)^{25,65,66,78,81}. Review articles^{64,85} suggest that a significant proportion of the available experimental data^{8,43,66,86} agrees well with the DE damping function, particularly for moderately entangled melts or solutions. This has been termed type A behaviour. A small number of studies, mostly in very weakly entangled fluids, show a weaker initial stress relaxation in the regime before the time-strain separable domain is reached, leading to a damping function that lies above the Doi-Edwards prediction (type B behaviour). Finally, studies⁶⁵ of fluids with high entanglement numbers $Z \gtrsim 50$ often report a faster stress relaxation before the time-strain separable domain is reached, so that the experimental damping function lies below that of Doi and Edwards^{8,43,44,86} (type C behaviour).

Velocimetric studies in this protocol commonly reveal ‘macroscopic motions’ following a step strain of sufficiently large amplitude $\gamma_0 \gtrsim 1.5$ in both entangled polymer melts and solutions^{9,13,28,49,72,88} and wormlike micelles¹². These macroscopic motions refer to non-zero velocities $v(y, t > t^*) \neq 0$ and associated heterogeneous shear zones – *i.e.*, shear bands – measured locally within the flow cell for some time even once the rheometer plates have stopped moving after the end of the ramp. Wang and co-workers showed that the same fluid can exhibit all three types of behaviour A to C above, depending on the extent of any wall slip associated with these ‘macroscopic motions’⁷²: bulk shear in the sample’s interior is usually associated with type A or B behaviour, and wall-slip with type C behaviour.

Theoretically, an instability leading to strain localisation following the imposition of a step strain was proposed in the context of the DE model by Marrucci and Grizzuti⁵⁸. The DE theory predicts a maximum in the shear stress $\Sigma(t', \gamma_0)$ when it is plotted as a function of applied strain amplitude γ_0 for a given time instant $t' \sim \tau_k$ after the step. This maximum occurs at a strain value of $\gamma_0 \approx 2$ and results in a negative slope for strain amplitudes beyond this maximum: $\partial_{\gamma_0} \Sigma(t' \sim \tau_k, \gamma_0) < 0$. Marrucci and Grizzuti used a free energy calculation to show that step strains with amplitudes in this regime of negative slope are unstable to the onset of heterogeneity.

Numerical studies of the rolie-poly model by Olmsted and co-workers have likewise reported shear rate hetero-

geneity during stress relaxation after a fast strain ramp of sufficiently large strain amplitude^{4,5} consistent with the predictions of Ref.⁵⁸. The form of this heterogeneity is sensitive to the initial noise conditions, and its onset can show a delay after the end of the ramp⁷. These results are in qualitative accordance with experiments showing that the onset of macroscopic motions can be delayed after the end of the ramp^{9,13,16}, with the delay time related to the time taken for polymer chain stretch to relax^{9,16}. Olmsted and co-workers also showed that in extreme cases a very large shear rate can develop across a stationary ‘fracture’ plane, so that the local velocity is very difficult to resolve. These results are qualitatively similar to experiments showing a ‘failure’ plane over which the shear rate is extremely high^{16,28}. Shear rate heterogeneity after a fast ramp has also been reported in a two species elastic network model⁹⁰.

C. Shear startup

In shear startup, a constant shear rate is applied to a previously undeformed sample for all times $t > 0$. Time-dependent shear banding has been widely reported in this protocol in entangled polymer solutions and melts^{13–16,41,73,75,83}, and in wormlike micelles^{12,40}. Its onset appears closely associated with the presence of an overshoot in the shear stress as it evolves from its initial value of zero to its final value on the ultimate steady state flow curve.

In some materials this time-dependent banding is effectively a precursor to true steady state banding. In such cases it can be viewed as the kinetic process by which these bands develop out of an initially homogeneous startup flow. Nonetheless, the magnitude of the time-dependent banding during startup is often strikingly greater than that which remains in the final steady state^{14,15,73,75,84}. Indeed, it is often sufficiently dramatic as to be accompanied by elastic-like recoil in which velocities measured locally within the flow cell can even temporarily become negative^{14,15,75} such that the fluid is locally and temporarily moving in the direction opposite to that of the rheometer plate that is driving the shear. Furthermore, pronounced but transient banding associated with a stress overshoot is also commonly seen even in less well entangled polymer solutions, for which the final steady flow state is homogeneous^{15,41,75}. Taken together, this evidence suggests that qualitatively different instability mechanisms might underlie shear banding in startup compared with that in steady state. We return to explore this concept in our discussion of ‘elastic’ versus ‘viscous’ banding instabilities in Sec. VII below.

Numerical studies have likewise reported time-dependent shear banding associated with stress overshoot in startup. Refs.^{3–5} explored the rolie-poly model of polymeric fluids, which can have either a monotonic or non-monotonic constitutive curve, depending the value of the convective constraint release parameter β and the entan-

gument number Z . This work demonstrated that banding and negative-velocity recoil can arise shortly after a stress overshoot, regardless of whether the underlying constitutive curve is monotonic or nonmonotonic. For a nonmonotonic constitutive curve this banding persists to steady state, though with a much weaker magnitude than during startup. For a monotonic constitutive curve, homogeneous flow is recovered in steady state. Ref.³ also discussed carefully the effects of rheometer cell curvature on these phenomena. Banding in startup has also been reported in simulations of a two-species elastic network model⁹⁰; and in molecular dynamics simulations of polymer melts¹⁹.

III. MODELS

A. Force balance

The stress response of a complex fluid to an applied deformation is dominated by the behaviour of its internal mesoscopic substructures⁴⁷. For example, a polymeric fluid comprises many chain-like molecules, the entanglements between which result in topological constraints on their molecular motion. We therefore decompose the total stress Σ into a viscoelastic contribution from these mesoscopic substructures, as well as a familiar Newtonian contribution of viscosity η , and an isotropic pressure:

$$\Sigma = G(\mathbf{W} - \mathbf{I}) + 2\eta\mathbf{D} - p\mathbf{I}. \quad (2)$$

The viscoelastic contribution $\sigma = G(\mathbf{W} - \mathbf{I})$ is expressed in terms of a constant elastic modulus G and a tensor $\mathbf{W}(\mathbf{r}, t)$, which describes the local conformation of the mesoscopic substructures. The dynamics of this conformation tensor in flow is prescribed by a viscoelastic constitutive equation. In the next section below we

introduce the constitutive equations that we shall use throughout this work. The Newtonian contribution $2\eta\mathbf{D}$ may arise from the presence of a true solvent, or may represent viscous stresses arising from any fast degrees of freedom of the polymer chains that are not ascribed to the viscoelastic contribution. Here $\mathbf{D} = \frac{1}{2}(\mathbf{K} + \mathbf{K}^T)$ where $K_{\alpha\beta} = \partial_\beta v_\alpha$ and $\mathbf{v}(\mathbf{r}, t)$ is the fluid velocity field. The isotropic pressure field $p(\mathbf{r}, t)$ is determined by the condition of incompressible flow:

$$\nabla \cdot \mathbf{v} = 0. \quad (3)$$

Throughout we consider the limit of zero Reynolds number, in which the force balance condition states that the stress tensor Σ must remain divergence free:

$$\nabla \cdot \Sigma = 0. \quad (4)$$

B. Viscoelastic constitutive equation

The rheological response of an entangled polymeric fluid can be modelled from a microscopic starting point by considering a test polymer chain that has its dynamics laterally constrained by topological entanglements with other chains. These entanglements are then represented in mean field spirit by an effective ‘tube’²⁶. The GLAMM model³⁴ provides a fully microscopic stochastic equation of motion for such a test chain and its tube. However it is computationally intensive to work with in practice. An approximation was therefore derived in Ref.⁵⁰ by projecting the full GLAMM model onto a single mode description, known as the rolie-poly (RP) model. This gives the viscoelastic constitutive equation for the dynamics of the conformation tensor as:

$$\partial_t \mathbf{W} + \mathbf{v} \cdot \nabla \mathbf{W} = \mathbf{K} \cdot \mathbf{W} + \mathbf{W} \cdot \mathbf{K}^T - \frac{1}{\tau_d} (\mathbf{W} - \mathbf{I}) - \frac{2(1-A)}{\tau_R} [\mathbf{W} + \beta A^{-2\delta} (\mathbf{W} - \mathbf{I})] + D\nabla^2 \mathbf{W}. \quad (5)$$

Here $A = \sqrt{3/T}$, where $T = \text{tr} \mathbf{W}$ denotes the magnitude of chain stretch. The reptation time τ_d is the timescale on which a test chain escapes its tube of constraints by undergoing 1D curvilinear diffusion along its own length. The Rouse time τ_R is the much shorter timescale on which chain stretch relaxes. The ratio of these two relaxation times is prescribed by the number of entanglements per chain²⁶ Z , with $\tau_d/\tau_R = 3Z$. The parameter β describes the efficacy of so-called convective constraint release (CCR) events, in which relaxation of polymer chain stretch also relaxes entanglement points, thereby also allowing relaxation of tube orientation. It has range $0 \leq \beta \leq 1$. The parameter δ also describes CCR. Following Ref.⁵⁰ we set $\delta = -\frac{1}{2}$ throughout. De-

pending on the values of the model parameters, the constitutive curve of the RP model can either be monotonic or non-monotonic.

The value of β is difficult to relate directly to experiment and there is no consensus on its correct value, though a small value was used by Likhtman and Graham to best fit experimental data⁵⁰ in flow protocols that were assumed to be homogeneous. A more recent study⁷ aimed at describing ‘fracture-like’ velocity profiles after a step strain likewise found a good fit to experimental findings only for small values of β .

The diffusive term $D\nabla^2 \mathbf{W}$ was absent in the original formulation of the model. Without it, however, the interface between the shear bands is unphysically sharp,

with a discontinuity in the shear rate profile $\dot{\gamma}(y)$ across it. Furthermore the total shear stress of a steady shear banded state is not uniquely selected, but depends on the shear history to which the material has been subject⁶³. This contradicts experimental findings, which find a unique plateau stress Σ_p . The diffusive term lifts this degeneracy to give a uniquely selected stress as well as a characteristic width to the interface between the bands of $\ell = O(\sqrt{D\tau_d})$ ^{51,63}.

A more phenomenologically motivated constitutive equation for concentrated polymeric solutions or melts considers an anisotropic drag on polymer chains that are oriented due to flow. Representing these chains simply as dumbbells, Giesekus³³ began with the upper convected Maxwell model for dilute solutions and incorporated into it an anisotropy parameter α with $0 \leq \alpha \leq 1$. The resulting constitutive equation has the form:

$$\partial_t \mathbf{W} + \mathbf{v} \cdot \nabla \mathbf{W} = \mathbf{K} \cdot \mathbf{W} + \mathbf{W} \cdot \mathbf{K}^T - \frac{1}{\lambda} (\mathbf{W} - \mathbf{I}) - \frac{\alpha}{\lambda} (\mathbf{W} - \mathbf{I})^2 + D \nabla^2 \mathbf{W}, \quad (6)$$

where λ is the relaxation time. A diffusive term is again included to properly describe a shear banding flow.

This Giesekus model admits either nonmonotonic or monotonic constitutive curves, depending on the value of α and the solvent viscosity η . It has been successful in modelling the steady state shear banding properties of entangled wormlike micelles^{36,37}, and a multimode equivalent has shown good agreement with the experimentally measured steady shear viscosity^{10,17,18,71} and damping function⁴⁵ of polymeric materials.

C. Flow geometry

Throughout we consider a sample of fluid sandwiched between parallel plates at $y = \{0, L\}$, sheared by moving the top plate in the \hat{x} direction. Translational invariance is assumed in the \hat{x}, \hat{z} directions. The fluid velocity is then of the form $\mathbf{v} = v(y, t) \hat{x}$, and the local shear rate

$$\dot{\gamma}(y, t) = \partial_y v(y, t). \quad (7)$$

The spatially averaged (or ‘global’) shear rate is

$$\bar{\dot{\gamma}}(t) = \frac{1}{L} \int_0^L \dot{\gamma}(y, t) dy. \quad (8)$$

D. Componentwise equations

In the flow geometry just described, the condition of incompressible flow (Eqn. 3) is automatically satisfied. The force balance condition of creeping flow (Eqn. 4) demands that the total shear stress is uniform across the cell $\partial_y \Sigma_{xy} = 0$. The viscoelastic and Newtonian solvent contributions may however each vary in space, provided their sum remains uniform:

$$\Sigma_{xy}(t) = G W_{xy}(y, t) + \eta \dot{\gamma}(y, t). \quad (9)$$

Componentwise the RP model reduces to a system of three dynamical variables:

$$\begin{aligned} \dot{W}_{xy} &= \dot{\gamma} W_{yy} - \frac{W_{xy}}{\tau_d} - \frac{2(1-A)}{\tau_R} (1 + \beta A) W_{xy} + D \partial_y^2 W_{xy}, \\ \dot{W}_{yy} &= -\frac{W_{yy} - 1}{\tau_d} - \frac{2(1-A)}{\tau_R} [W_{yy} + \beta A (W_{yy} - 1)] + D \partial_y^2 W_{yy}, \\ \dot{T} &= 2\dot{\gamma} W_{xy} - \frac{T - 3}{\tau_d} - \frac{2(1-A)}{\tau_R} [T + \beta A (T - 3)] + D \partial_y^2 T. \end{aligned} \quad (10)$$

In the limit of fast chain stretch relaxation $\tau_R \rightarrow 0$ this reduces to a simpler system of two dynamical variables:

$$\begin{aligned} \dot{W}_{xy} &= \dot{\gamma} \left[W_{yy} - \frac{2}{3} (1 + \beta) W_{xy}^2 \right] - \frac{1}{\tau_d} W_{xy} + D \partial_y^2 W_{xy} \\ \dot{W}_{yy} &= \frac{2}{3} \dot{\gamma} [\beta W_{xy} - (1 + \beta) W_{xy} W_{yy}] - \frac{1}{\tau_d} (W_{yy} - 1) + D \partial_y^2 W_{yy}. \end{aligned} \quad (11)$$

with a constant molecular trace $T = 3$. We shall refer to this ‘non-stretching’ form below as the nRP model; and

the full ‘stretching’ version of Eqns. 10 as the sRP model.

The Giesekus model likewise reduces to a system of

three dynamical variables:

$$\begin{aligned}
\dot{W}_{xy} &= \dot{\gamma}W_{yy} - \frac{W_{xy}}{\lambda} - \frac{\alpha W_{xy}}{\lambda} [(W_{xx} - 1) + (W_{yy} - 1)] + D\partial_y^2 W_{xy}, \\
\dot{W}_{xx} &= 2W_{xy}\dot{\gamma} - \frac{W_{xx} - 1}{\lambda} - \frac{\alpha}{\lambda} [W_{xy}^2 + (W_{xx} - 1)^2] + D\partial_y^2 W_{xx}, \\
\dot{W}_{yy} &= -\frac{W_{yy} - 1}{\lambda} - \frac{\alpha}{\lambda} [W_{xy}^2 + (W_{yy} - 1)^2] + D\partial_y^2 W_{yy}.
\end{aligned} \tag{12}$$

We note an important distinction in the structure of these equations. In particular, in the stretching rolie-poly model Eqns. 10 and the Giesekus model Eqns. 12, the terms prefactored by $\dot{\gamma}$ are of simple linear form, whereas the terms prefactored by the inverse relaxation timescales are nonlinear. Conversely in the nonstretch rolie-poly model the terms prefactored by $\dot{\gamma}$ are nonlinear, whereas the terms prefactored by the inverse relaxation timescales are linear. Because the terms prefactored by $\dot{\gamma}$ dominate the response of a material to a fast shear startup and fast strain ramp, this distinction will be important in what follows, particularly with regards the onset of what we shall term ‘elastic instability’.

E. General framework

Motivated by the preceding discussion, we now outline a general theoretical framework for the planar shear flow of complex fluids. This will encompass as special cases the rolie-poly and Giesekus models just described, as well as many other models for the rheology of complex fluids. It is within this general framework that we shall below perform a linear stability analysis to derive fluid-universal criteria for the onset of shear banding in time-dependent flows⁶¹. Accordingly, the results that we obtain should apply to all complex fluids that can be described by a rheological constitutive equation of the highly general form that we propose here.

We begin by combining all dynamical variables relevant to the fluid in question into a state vector \mathbf{s} . In a polymeric fluid this will include all components of the viscoelastic conformation tensor \mathbf{W} discussed above, $\mathbf{s} = (W_{xy}, W_{xx}, W_{yy}, \dots)^T$. In soft glassy materials it would also include fluidity variables capable of describing the slow evolution of a material into a progressively more solid-like state³⁰.

Next we define a projection vector $\mathbf{p} = (1, 0, 0, \dots)$ to select out of this state vector the shear component W_{xy} of the viscoelastic conformation variable. The total shear stress $\Sigma_{xy} = \Sigma$ is then written:

$$\Sigma(t) = G\mathbf{p} \cdot \mathbf{s}(y, t) + \eta\dot{\gamma}(y, t). \tag{13}$$

Here and below we drop the xy subscript from the shear component Σ of the total stress for clarity.

In a planar shear flow, the viscoelastic constitutive equation has the generalised form

$$\partial_t \mathbf{s} = \mathbf{Q}(\mathbf{s}, \dot{\gamma}) + D\partial_y^2 \mathbf{s}. \tag{14}$$

The choice of constitutive model then specifies the functional form of \mathbf{Q} . Depending on this choice we can obtain, for example, the rolie-poly⁵⁰, Giesekus³³, Johnson-Segalman⁸⁷ or (for an infinite dimensional \mathbf{s}) soft glassy rheology model³⁵ and many more besides. The compact notation introduced in this subsection therefore includes the behaviour in shear of any fluid described in subsections A - D above. Crucially, however, we shall not need to specify \mathbf{Q} in order to perform our linear stability analysis for the onset of banding. Our stability results will therefore be generic to all models described by a constitutive equation of this highly general form.

F. Units and parameters

Throughout we choose units in which the rheometer gap width $L = 1$; the elastic modulus $G = 1$; and the terminal viscoelastic relaxation time $\tau_d = 1$ (RP model) or $\lambda = 1$ (Giesekus model).

In our nonlinear simulations we shall set the value of the diffusion constant D such that the interface between the bands has a typical lengthscale $\ell = 10^{-2}L$. In our linear stability analysis we neglect the diffusive terms since they do not affect the results for the long wavelength modes of interest here.

This leaves as parameters to be explored the solvent viscosity η , the CCR parameter β (nRP and sRP models), the stretch relaxation time τ_R (sRP model) and the anisotropy parameter α (Giesekus model).

IV. LINEAR STABILITY ANALYSIS

In this section we outline a linear stability analysis to determine whether a state of initially homogeneous shear flow, which we shall call the underlying ‘base state’, becomes unstable to the growth of heterogeneous perturbations that are the precursor of a shear banded state. Distinct from more conventional linear stability analyses, we are concerned here with a base state that

is time-dependent, comprising the initially homogeneous dynamical response of the fluid following the imposition of a step stress, step strain, or shear startup. Accordingly, our analysis follows previous time-dependent ones in Refs.^{3,31,57}.

A. Equations of motion for heterogeneous perturbations

Working within the general framework set out in Sec. III E above, we start by expressing the response of the system to the imposed flow protocol (step stress, strain ramp, shear startup) as the sum of a time-dependent homogeneous base state plus any (initially) small heterogeneous perturbations:

$$\begin{aligned}\Sigma(t) &= \Sigma_0(t), \\ \dot{\gamma}(y, t) &= \dot{\gamma}_0(t) + \sum_{n=1}^{\infty} \delta\dot{\gamma}_n(t) \cos(n\pi y/L), \\ \mathbf{s}(y, t) &= \mathbf{s}_0(t) + \sum_{n=1}^{\infty} \delta\mathbf{s}_n(t) \cos(n\pi y/L).\end{aligned}\quad (15)$$

The first of these equations lacks the heterogeneous perturbations seen in the other two because the total shear stress must remain uniform across the sample, according to the force balance condition. The time-dependence of the base state is clearly such that in a step stress protocol $\Sigma_0(t) = \Sigma_0 = \text{const.}$; during a strain ramp $\dot{\gamma}_0(t) = \dot{\gamma}_0 = \text{const.}$ with $\dot{\gamma}_0 = 0$ post-ramp; and during a shear startup $\dot{\gamma}_0(t) = \dot{\gamma}_0 = \text{const.}$

Substituting Eqns. 15 into Eqns. 13 and 14, neglecting the diffusive terms as noted above, and expanding in successive powers of the magnitude of the small perturbations $\delta\dot{\gamma}_n, \delta\mathbf{s}_n$, we find at zeroth order that the homogeneous base state obeys:

$$\begin{aligned}\Sigma_0(t) &= G\mathbf{p} \cdot \mathbf{s}_0(t) + \eta\dot{\gamma}_0(t), \\ \dot{\mathbf{s}}_0 &= \mathbf{Q}(\mathbf{s}_0, \dot{\gamma}_0).\end{aligned}\quad (16)$$

At first order, the heterogeneous perturbations obey

$$\begin{aligned}0 &= G\mathbf{p} \cdot \delta\mathbf{s}_n(t) + \eta\delta\dot{\gamma}_n(t), \\ \dot{\delta\mathbf{s}}_n &= \mathbf{M}(t) \cdot \delta\mathbf{s}_n + \mathbf{q}\delta\dot{\gamma}_n,\end{aligned}\quad (17)$$

in which $\mathbf{M} = \partial_{\mathbf{s}} \mathbf{Q}|_{\mathbf{s}_0, \dot{\gamma}_0}$ and $\mathbf{q} = \partial_{\dot{\gamma}} \mathbf{Q}|_{\mathbf{s}_0, \dot{\gamma}_0}$. These two linearised equations can be combined to give

$$\dot{\delta\mathbf{s}}_n = \mathbf{P}(t) \cdot \delta\mathbf{s}_n, \quad (18)$$

in which

$$\mathbf{P}(t) = \mathbf{M}(t) - \frac{G}{\eta} \mathbf{q}(t) \mathbf{p}. \quad (19)$$

We neglect terms of second order and above.

In what follows our first objective will be to determine whether at any time t the heterogeneous perturbations $\delta\dot{\gamma}_n, \delta\mathbf{s}_n(t)$ have a negative or positive rate of growth, respectively indicating linear stability or instability to the

onset of shear banding. Our second objective is to relate the onset of growth in these heterogeneous perturbations – *i.e.*, the onset of shear banding – to any distinctive signature in the shape of the experimentally measured rheological response function as specified by the evolution of the underlying homogeneous base state in any given protocol.

We shall tackle these objectives using three different methods that we cross-check against each other. First, we denote by $\omega(t)$ the real part the eigenvalue of $\mathbf{P}(t)$ that has the largest real part at any time t . A positive $\omega(t)$ strongly suggests that heterogeneous perturbations will be instantaneously growing at that time t . This concept of a time-dependent eigenvalue must, however, be treated with caution⁸². Therefore second, and better, we directly integrate the linearised Eqns. 18 using an Euler time-stepping method, carefully converged with respect to reducing the timestep. We examine the time-evolution of the heterogeneous perturbations thereby calculated, to see whether at any instant they are growing or decaying. Finally, we integrate the full non-linear spatio-temporal Eqns. 13 and 14 using a Crank Nicolson algorithm⁷⁰, carefully checked for convergence with respect to the size of the time- and space-steps. The heterogeneous part of the solution of this third method must coincide with the results of the second method as long as the system remains in the linear regime of small perturbations.

As written above, the stability matrix \mathbf{P} appears to show no dependence on the spatial lengthscale of the perturbation, as denoted by n . The same comment therefore applies to the eigenvalues of \mathbf{P} . This follows from our having neglected the diffusive term in the viscoelastic constitutive equation before performing the linearisation. Reinstating the diffusive term would simply transform any eigenvalue $\omega \rightarrow \omega_n = \omega - Dn^2\pi^2/L^2$ and act to damp out any perturbations with a wavelength of order the microscopic lengthscale l or below. Accordingly the results of our stability analysis apply only to perturbations of macroscopic lengthscale, which are the ones of interest in the initial formation of shear bands.

B. Seeding the heterogeneous perturbations

So far, we have discussed how to determine whether heterogeneous perturbations to the homogeneous base state grow or decay over time. We now consider how such perturbations are seeded into the system in the first place. We identify several different possible physical mechanisms for this, including (a) residual heterogeneities that remain in the fluid following initial sample preparation, (b) imperfect rheometer feedback or plate alignment, (c) true thermal noise, or (d) slight rheometer device curvature in a curved Couette or cone-and-plate geometry, which adds a small systematic perturbation to the componentwise equations that we wrote above within the assumption of a theoretically idealised planar geometry.

Of these, we model (a) by adding a small heterogeneous perturbation once only, before the onset of deformation, by initialising $\delta \mathbf{s}_n(t=0) = q\mathbf{X}\delta_{n1}$ for the Fourier modes of the linearised equations, or correspondingly $\delta \mathbf{s}(y, t=0) = q\mathbf{X} \cos(n\pi y/L)$ with $n=1$ in the full spatio-temporal equations. (δ_{nm} is the Kronecker delta function, equal to 1 if $n=m$ and equal to 0 otherwise.) This initial perturbation has magnitude q , which we treat as a parameter of our study. \mathbf{X} is a vector of the same dimension as the vector \mathbf{s} . Each of its components is a random number drawn from a uniform distribution of mean 0 and width 1. We choose to seed only the lowest mode $n=1$ because it is always the most unstable (or least stable) one: as discussed above, the diffusive terms render modes of higher n less unstable (or more stable).

The results presented below follow the method of seeding (a) just described unless otherwise stated. In some cases we also check these results against scenarios (b) and (c), modelled by adding a small heterogeneous perturbation $q\sqrt{dt}\mathbf{X}\delta_{n1}$ at every timestep (of duration dt) to the Fourier modes of the linearised equations, or correspondingly $q\sqrt{dt}\mathbf{X} \cos(\pi y/L)$ at every timestep in the full spatio-temporal simulation. A new random vector \mathbf{X} is selected at each timestep. In this case we first evolve the system under conditions of no applied flow or loading but subject to this continuous noise, until a statistically steady state is reached that correctly captures the fluctuation spectrum of the system in zero shear. We then evolve the chosen flow protocol, also subject to this continuous noise.

For the linearised equations subject to continuous noise, it is furthermore possible to perform an upfront analytical average (denoted $\langle \rangle$) over infinitely many noise histories by evolving the variance of the perturbations:

$$\partial_t \mathbf{S} = \mathbf{P} \cdot \mathbf{S} + \mathbf{S} \cdot \mathbf{P}^T + \mathbf{N}, \quad (20)$$

in which $\mathbf{S}(t) = \langle \delta \mathbf{s}_n(t) \cdot \delta \mathbf{s}_n^T(t) \rangle$ and $\mathbf{N}(t)$ is a diagonal matrix characterising the amplitude of the added noise. Using the linearised force balance condition we then easily obtain the evolution of the variance of the shear rate perturbations $\langle \delta \dot{\gamma}_n^2 \rangle(t)$.

C. Reporting the heterogeneous perturbations

For the linearised system subject to seeding (a) above we report the size of the shear rate heterogeneity as $|\delta \dot{\gamma}_{n=1}|(t)$. For a linearised system subject to continuous noise (b, c) we report $\sqrt{\langle \delta \dot{\gamma}_{n=1}^2 \rangle}(t)$. In the full nonlinear spatiotemporal simulation we quantify the degree of heterogeneity by the difference at any time between the maximum and minimum values of the shear rate across the cell:

$$\Delta_{\dot{\gamma}}(t) = \dot{\gamma}_{\max} - \dot{\gamma}_{\min}. \quad (21)$$

We often below refer to this quantity as the ‘degree of banding’.

We have checked that as long as the nonlinear simulation remains in the linear regime of small heterogeneity, the $\Delta_{\dot{\gamma}}$ that it predicts evolves in the same way as the perturbations calculated in the corresponding linearised calculation, up to a constant prefactor $O(1)$.

V. RESULTS: STEP STRESS

In this section we present our results for time-dependent shear banding during a system’s creep response following the imposition of a step shear stress to a previously unloaded sample, $\Sigma(t) = \Sigma_0 \Theta(t)$. We start in Sec.V A by developing an analytical criterion for the onset of banding. In Secs. V B and V C we give numerical results to support this prediction, in the rolie-poly and Giesekus models respectively.

A. Criterion for shear banding following a step stress

Here we develop a criterion for the onset of shear banding in the step stress protocol. We do so by considering an underlying base state of initially homogeneous flow response to the applied loading, and the dynamics of small heterogeneous perturbations about this base state.

Following the imposition of a step shear stress to a previously unloaded sample, it is easy to show by time-differentiating Eqns. 16 subject to the constraint $\Sigma_0(t) = \Sigma_0$ that any underlying base state of initially homogeneous flow response must obey

$$\frac{d}{dt} \dot{\mathbf{s}}_0 = (\mathbf{M} - G\mathbf{q}\mathbf{p}/\eta) \cdot \dot{\mathbf{s}}_0. \quad (22)$$

Eqns. 18 and 19 together show that any heterogeneous perturbations to this base state must obey

$$\frac{d}{dt} \delta \mathbf{s}_n = (\mathbf{M} - G\mathbf{q}\mathbf{p}/\eta) \cdot \delta \mathbf{s}_n. \quad (23)$$

Comparing these two equations, we see that the heterogeneous perturbations $\delta \mathbf{s}_n$ obey the same dynamical equation as the time-derivative of the homogeneous base state $\dot{\mathbf{s}}_0$. Combined with the force balance condition (Eqn. 4) and its linearised counterpart, this means that heterogeneous shear rate perturbations must grow, and shear bands develop,

$$\frac{d\delta \dot{\gamma}_n}{dt} / \delta \dot{\gamma}_n > 0, \quad (24)$$

in any regime where

$$\frac{d^2 \dot{\gamma}_0}{dt^2} / \frac{d\dot{\gamma}_0}{dt} > 0. \quad (25)$$

This important result tells us that a state of initially homogeneous creep response to an imposed step stress becomes linearly unstable to the onset of shear banding whenever its shear rate signal $\dot{\gamma}_0(t)$ is simultaneously

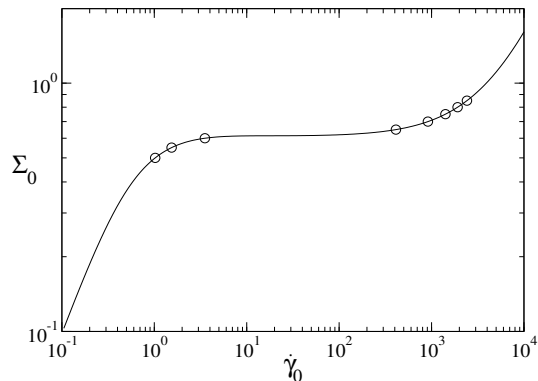


FIG. 3. Steady state constitutive curve in the rolie-poly model. Symbols correspond to steady states from Fig. 4. Parameters: $\beta = 0.8$, $\eta = 10^{-4}$, $\tau_R = 0.0$.

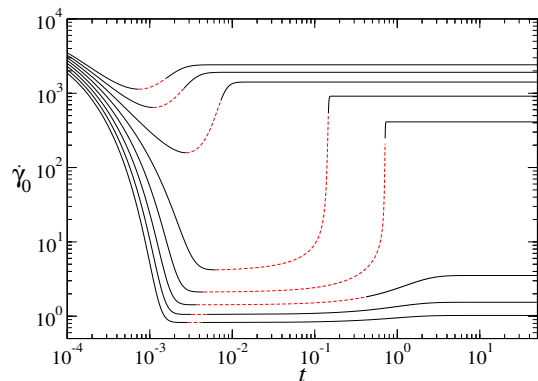


FIG. 4. Shear rate as a function of time for imposed shear stresses $\Sigma_0 = 0.5, 0.55, \dots, 0.85$ (curves bottom to top at fixed t) in the (homogeneously constrained) RP model. Dashed lines show regions of linear instability, $\partial_t^2 \dot{\gamma}_0 / \partial_t \dot{\gamma}_0 > 0$. Steady states correspond to the circles in Fig. 3. Parameters: $\beta = 0.8$, $\eta = 10^{-4}$, $\tau_R = 0.0$.

upwardly curving and upwardly sloping in time. (Alternatively $\dot{\gamma}_0(t)$ may be simultaneously downwardly curving and downwardly sloping, though in practice we have never seen this numerically.)

How does this time-differentiated creep curve $\dot{\gamma}_0(t)$ of the underlying homogeneous base state relate to the time-differentiated creep curve $\bar{\gamma}(t)$ measured experimentally by recording the motion of the rheometer plates? Clearly, in any regime before banding sets in these two quantities coincide by definition. Once shear banding fluctuations have grown appreciably into the nonlinear regime, however, the two need not coincide. Nevertheless, in our numerical studies of step stress in the rolie-poly and Giesekus models (and also of the soft glassy rheology model reported elsewhere³⁰) we have never observed the globally measured bulk shear rate signal to be strongly affected, in overall shape at least, by the presence of shear banding within the fluid. Accordingly we can take Eqn. 25 to apply also to the experimentally measured signal $\bar{\gamma}(t)$. Experimentalists should therefore be

alert to the onset of shear banding in any creep experiment where the time-differential of the measured creep curve simultaneously shows upward slope and upward curvature: bulk rheological data can be used as a predictor of the presence of shear banding, even in the absence of accompanying velocimetric data.

B. Numerical results: rolie-poly model

Having developed an analytical criterion for the onset of shear banding following the imposition of a step stress, we now present numerical results that support it. Fig. 3 shows the underlying constitutive curve of stress as a function of strain rate in the rolie-poly model for a value of the CCR parameter $\beta = 0.8$. Because this curve is monotonic, the eventual steadily flowing state is homogeneous.

Nonetheless for imposed stress values in the relatively flat region of this curve, we might expect shear bands to form transiently as the system evolves towards its steady state on this ultimate constitutive curve. Motivated by this expectation, we now study numerically the step stress protocol for the stress values denoted by circles in Fig. 3.

We report first results for the underlying time-dependent base state of homogeneous creep response to this imposed load, obtained in a numerical calculation in which the flow is artificially constrained to remain homogeneous. The shear rate evolution $\dot{\gamma}_0(t)$ in this case is shown in Fig. 4. Immediately after loading the solvent bears all the applied stress and $\dot{\gamma}_0(t = 0^+) = \Sigma_0/\eta$. The shear rate then shows a rapid early decay on a timescale that appears numerically to scale as $O(\sqrt{\eta \tau_d / G})$, but that may not be accessible experimentally due to inertial effects such as creep ringing that we have neglected here. (Our numerics set any inertial timescales to zero.) Following this fast initial drop, the shear rate subsequently displays a regime of simultaneous upwards curvature and upwards slope, shown by dashed lines in the figure. In this regime, this underlying base state of homogeneous flow is predicted by our criterion (25) above to become linearly unstable to the onset of shear rate heterogeneity.

Accordingly, in Figure 5a-c) we show the results of a fully nonlinear simulation that now permits heterogeneity in the flow-gradient direction. Subfigure (a) shows the evolution of the global shear rate $\bar{\gamma}(t)$ for a single stress value $\Sigma = 0.7$, near the point of weakest slope of the constitutive curve in Fig. 4. As can be seen, this bulk rheological signal differs little from that given by our earlier homogeneous calculation: $\bar{\gamma}(t) \approx \dot{\gamma}_0(t)$, even in the regime where bands form and the two signals might be expected to differ. This supports our claim made above that the theoretical criterion of Eqn. 25, which strictly applies only to the underlying base state $\dot{\gamma}_0(t)$, can also be applied to the experimentally measured bulk signal $\bar{\gamma}(t)$.

Subfigure (b) shows snapshots of the velocity profiles

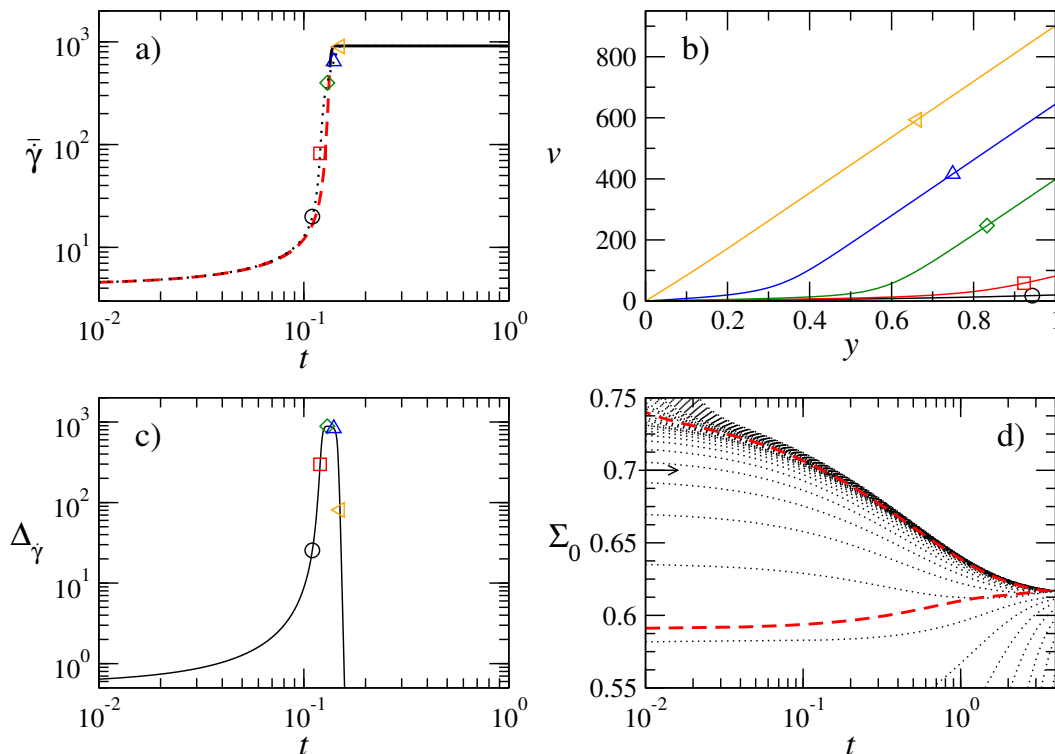


FIG. 5. Step stress of amplitude $\Sigma_0 = 0.7$ in the RP model: (a) Thick line: global shear rate in a homogeneously constrained system, with the dashed region denoting $\partial_t^2 \dot{\gamma}_0 / \partial_t \dot{\gamma}_0 > 0$. Dotted line shows corresponding signal with heterogeneity allowed, $\bar{\gamma}$. (b) Snapshots of the velocity profile at times corresponding to symbols in (a). (c) Corresponding degree of banding: $\Delta_{\dot{\gamma}} = \dot{\gamma}_{\max} - \dot{\gamma}_{\min}$. (d) Banding dynamics in the full plane of stress versus time. A horizontal slice across this plane corresponds to a single run at a constant imposed stress Σ_0 , in which we integrate the linearised equations for the dynamics of the heterogeneous perturbations. Dotted lines are contours of equal $|\delta\dot{\gamma}|_{n=1}(t) = |\delta\dot{\gamma}|_{n=1}(0)2^M$ for integer M . (We show only contours $M > -50$, thereby cutting off the final stage of the decay at the right hand side of the graph.) The thick dashed line shows where the base state $\partial_t^2 \dot{\gamma}_0 / \partial_t \dot{\gamma}_0 = 0$, with linear instability to the left of it. The arrow denotes the stress value explored in detail in subfigures (a) to (c). Parameters: $\beta = 0.8$, $\eta = 10^{-4}$, $\tau_R = 0.0$, $q = 0.1$.

that accompany the bulk signal of (a). These clearly exhibit macroscopic shear banding. Plotting the associated degree of banding $\Delta_{\dot{\gamma}}(t) = \dot{\gamma}_{\max} - \dot{\gamma}_{\min}$ as a function of time in (c), we find good agreement with our prediction (25). Banding sets in once $\bar{\gamma}$ shows upward curvature. The flow then returns to be homogeneous once $\bar{\gamma}$ exhibits downward curvature during the final stage of its evolution to steady state.

Subfigure 5d) summarises the shear banding dynamics of the system across a range of stress values, in the plane of stress versus time. Any horizontal slice across this plane represents a single creep run at a constant value of the imposed stress Σ , as discussed in subfigures (a)-(c). The thick dashed line encloses to its left the regime of linear instability to the onset of banding, in which heterogeneous shear rate perturbations are predicted to grow. This line is obtained by applying our criterion (25) to the base state signal calculated numerically in a series of runs at closely spaced values of the imposed stress. To make an exploration of the dynamics of shear banding perturbations feasible in this full plane of stress versus time, we integrated the linearised equa-

tions of motion (23). (Performing the full nonlinear and spatially aware simulation across a wide range of closely spaced stress values would be much more time consuming computationally.) The dotted lines show contours of equal $|\delta\dot{\gamma}|_{n=1}(t) = |\delta\dot{\gamma}|_{n=1}(0)2^M$ for integer M . The region of growth in these perturbations agrees well with our analytical criterion enclosed by the dashed line. It corresponds to stress values $0.61 \lesssim \Sigma \lesssim 0.75$ around the region of weakest slope of the constitutive curve.

Time-dependent shear banding during a sharp increase in the shear rate response $\bar{\gamma}(t)$ following the imposition of a step stress has been reported experimentally in polymeric systems in Refs.^{12,14,15,38-41,83}.

The results in Fig. 5 apply to a system in which a heterogeneous perturbation is seeded once only, at the initial time $t = 0$. In practice, such a situation might correspond to the sample being left in a slightly heterogeneous state as a result of the experimental protocol by which it is initially loaded into the rheometer. Alternatively, perturbations may be seeded continuously during the experiment due to imperfect rheometer feedback. To model this we also performed calculations in which small

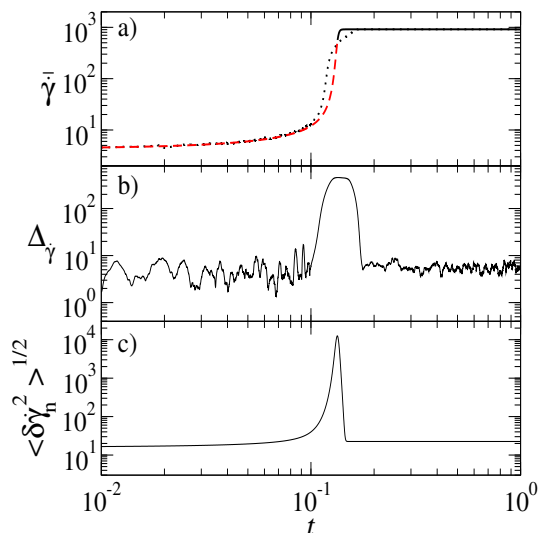


FIG. 6. Step stress in the RP model with noise added at each timestep. (a) Thick line: global shear rate $\dot{\gamma}_0$ in a homogeneously constrained system, with the dashed region denoting $\partial_t^2 \dot{\gamma}_0 / \partial_t \dot{\gamma}_0 > 0$. Dotted line shows corresponding signal with heterogeneity allowed $\bar{\dot{\gamma}}$. (b) Degree of shear banding: $\Delta_{\dot{\gamma}} = \dot{\gamma}_{\max} - \dot{\gamma}_{\min}$ from a fully nonlinear simulation with $q = 0.1$. (Here a running average over data captured at frequent points in time is used, checked for qualitative convergence with respect to the capture frequency and running average range.) (c) Shear rate perturbation $\sqrt{\langle \delta \dot{\gamma}_n^2 \rangle}$ of the linearised system found by integrating Eqn 20. Magnitude of noise $q = 10^{-5}$. Values of model parameters as in Fig. 5.

heterogeneous perturbations are added at every timestep. Pleasingly, we find qualitatively similar results: compare Figs. 5 and 6.

C. Numerical results: Giesekus model

We now discuss our numerical results for an imposed step stress in the Giesekus model. To ensure a fair comparison with our study of the rolie-poly model just described, we use a value of the anisotropy parameter α such that the underlying constitutive curve is monotonic and as closely resembling that of Fig. 3 as possible. Also as before, we set our value for the imposed stress to be in the region of weakest slope in this curve.

The shape of the shear rate response to this imposed step stress is qualitatively similar to that seen in the RP model, in particular in showing a regime of upward curvature. Compare Figs. 6a) and 7a). In principle this upward curvature renders a state of initially homogeneous flow unstable to the development of shear bands. Indeed, shear rate heterogeneities do start to grow as a result of this linear instability. However we have never found them to grow sufficiently large as to give ‘significant’ shear banding in our numerical simulations of the Giesekus model. The degree of banding $\Delta_{\dot{\gamma}}(t) = \dot{\gamma}_{\max} - \dot{\gamma}_{\min}$ never exceeds 5% of the global shear rate $\bar{\dot{\gamma}}(t)$ averaged across

the sample, and thus would be hard to detect experimentally¹. Contrast the results for $\Delta_{\dot{\gamma}}(t)$ and $v(y)$ in Fig. 7 with their counterpart for the RP model in Fig. 5c). By repeating this numerical calculation across a wide range of values of α, η , and Σ_0 , we checked that this conclusion of negligible banding is general for this protocol in the Giesekus model.

The reason for this striking difference in shear banding behaviour between the two models, despite their differentiated creep response curves $\dot{\gamma}_0(t)$ having the same upwardly curving shape, is that the maximal value of the curvature in $\dot{\gamma}(t)$ is always much smaller in the Giesekus model than the RP model. Compare Figs. 5a) and 7a). Correspondingly, the resulting maximum degree of shear banding is much smaller.

In Fig. 7, heterogeneous perturbations are seeded once only, at the initial time $t = 0$. By comparison in Fig. 8 the system is first evolved to steady state at $\Sigma = 0$ with small perturbations added at every timestep, before being evolved at the chosen $\Sigma = \Sigma_0$ with perturbations again added continuously at every timestep. Although we never found ‘significant banding’ ($> 5\%$) in the Giesekus model with this noise history either, there is nonetheless an interesting feature not seen in the RP model. In particular, the amplitude of heterogeneity in steady flow is much greater than in the unsheared system at rest. (In contrast, in the RP model the magnitude of heterogeneity in steady shear is comparable to that in zero shear, recall Fig. 6.) Whether or not these fluctuations would be large enough to be detected by sensitive velocimetry, this remains an interesting feature of the Giesekus model.

VI. RESULTS: STRAIN RAMP

In this section we consider a strain ramp protocol in which a previously undeformed sample is subject to an applied shear at rate $\dot{\gamma}_0$ by moving the top plate at speed $\dot{\gamma}_0 L$ for times $0 < t < t^*$. After this the plate is held fixed, giving a total applied strain amplitude $\gamma^* = \dot{\gamma}_0 t^*$. The limit $\dot{\gamma}_0 \rightarrow \infty, t^* \rightarrow 0$ at fixed γ^* gives a theoretically idealised step strain. We focus here on ramp rates that are finite but nonetheless always fast compared to the terminal relaxation time. Therefore we impose $\dot{\gamma}_0 \tau_d \gg 1$ in the RP model and $\dot{\gamma}_0 \lambda \gg 1$ in the Giesekus model. (For the RP model, we then separately distinguish between ramps for which $\dot{\gamma}_0 \tau_R \ll 1$ and $\dot{\gamma}_0 \tau_R \gg 1$.) Following such fast ramps, we develop a criterion for the transient appearance of shear bands as the system relaxes back to equilibrium post-ramp.

A. Criterion for instability after a fast strain ramp

We start by writing our general governing Eqns. 13 and 14 in a form that emphasizes the additive loading and relaxation dynamics that obtain in all constitutive

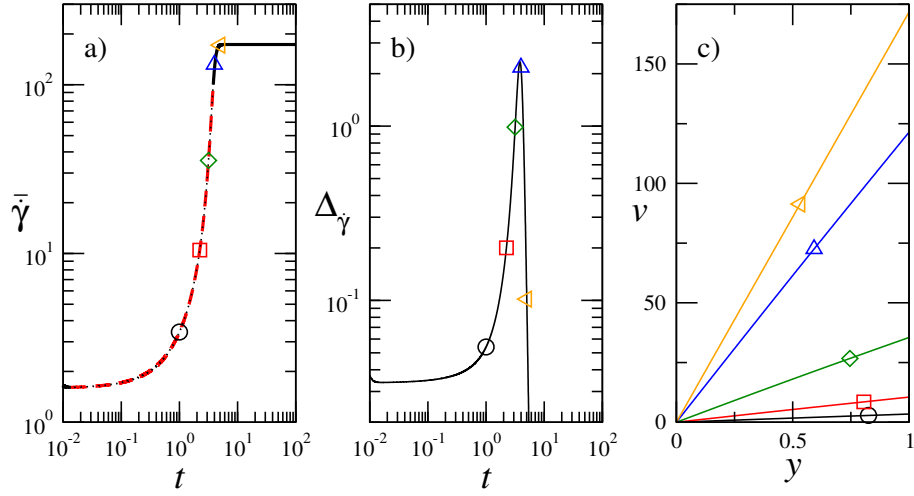


FIG. 7. Step stress in the Giesekus model. (a) Thick line: shear rate response in a homogeneously constrained system, with the dashed region denoting $\partial_t^2 \dot{\gamma}_0 / \partial_t \dot{\gamma}_0 > 0$. Dotted line shows corresponding signal with heterogeneity allowed, which is now indistinguishable from the homogeneous signal. (b) Degree of banding: $\Delta\dot{\gamma} = \dot{\gamma}_{\max} - \dot{\gamma}_{\min}$. (c) Snapshots of the velocity profile at times corresponding to symbols in (a) and (b). Parameters: $\alpha = 0.6$, $\eta = 10^{-3}$, $\Sigma = 1.0$, $q = 0.1$.

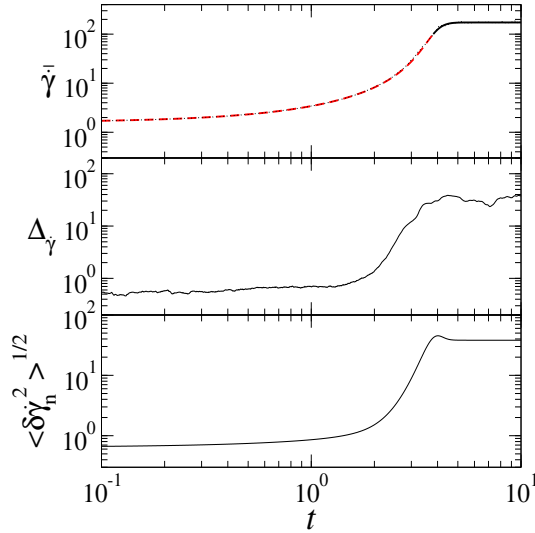


FIG. 8. Step stress in the Giesekus model with parameters as in Figure 7. Top: Thick line shows the shear rate $\dot{\gamma}_0$ in a homogeneously constrained system, with the dashed region denoting $\partial_t^2 \dot{\gamma}_0 / \partial_t \dot{\gamma}_0 > 0$. Dotted line shows corresponding signal with heterogeneity allowed $\bar{\dot{\gamma}}$, now indistinguishable from the homogeneous signal. Middle: degree of shear banding: $\Delta\dot{\gamma} = \dot{\gamma}_{\max} - \dot{\gamma}_{\min}$ from the nonlinear simulation with $q = 0.1$ (Here a running average over data captured at frequent points is used, checked for qualitative convergence with respect to the capture frequency and running average range.) Bottom: Shear rate perturbation $\sqrt{\langle \delta\dot{\gamma}_n^2 \rangle}$ in linearised system found by integrating Eqns. 20, $q = 10^{-5}$.

equations of which we are aware:

$$\Sigma(t) = G\mathbf{p} \cdot \mathbf{s}(y, t) + \eta\dot{\gamma}(y, t), \quad (26)$$

$$\partial_t \mathbf{s} = \dot{\gamma}\mathbf{S}(\mathbf{s}) - \frac{1}{\tau}\mathbf{R}(\mathbf{s}). \quad (27)$$

Here τ is the terminal relaxation time. (Two relaxation times, as in the sRP model, are included in this notation by writing $\mathbf{R} = \mathbf{R}_1 + \frac{\tau}{\tau_R}\mathbf{R}_2$.) For the purposes of the linear stability calculation that follows we have neglected small diffusive terms in Eqn. 27, as discussed above.

To develop our criterion for the onset of shear banding we follow our usual linear stability procedure of considering an underlying base state of initially homogeneous flow response to the imposed deformation, and the dynamics of heterogeneous perturbations to this base state that might grow into observable shear banding.

Accordingly we write

$$\begin{aligned} \Sigma(t) &= \Sigma_0(t), \\ \dot{\gamma}(y, t) &= \dot{\gamma}_0(t) + \sum_{n=1}^{\infty} \delta\dot{\gamma}_n(t) \cos(n\pi y/L), \\ \mathbf{s}(y, t) &= \mathbf{s}_0(t) + \sum_{n=1}^{\infty} \delta\mathbf{s}_n(t) \cos(n\pi y/L). \end{aligned} \quad (28)$$

We then substitute these into the governing equations (26) and (27), and expand in successive powers of the amplitude of the perturbations.

The zeroth order equations in this expansion govern the evolution of the base state. During the ramp this evolves according to

$$\begin{aligned} \frac{d\mathbf{s}_0}{d\dot{\gamma}_0} &= \mathbf{S}(\mathbf{s}_0) - \frac{1}{\tau\dot{\gamma}_0}\mathbf{R}(\mathbf{s}_0) \\ &\approx \mathbf{S}(\mathbf{s}_0). \end{aligned} \quad (29)$$

In the second line we have specialised to the fast ramps of interest here, for which the loading dynamics dominates. Denoting the base state immediately as the ramp ends $\mathbf{s}_0(t = t^{*-}) = \mathbf{s}_0^*$, the dynamics of the base state

immediately prior to the end of the ramp obeys

$$\frac{ds_0}{d\gamma_0} \Big|_{t^{*-}} = \mathbf{S}(s_0^*). \quad (30)$$

Post-ramp the base state relaxes back to equilibrium according to

$$\frac{ds_0}{dt} = -\frac{1}{\tau} \mathbf{R}(s_0). \quad (31)$$

Having discussed the evolution of the underlying homogeneous base state we now turn to the linearised dynamics of the heterogeneous perturbations. These are specified by the first order equations in the amplitude expansion just discussed. (Recall Eqns. 18 and 19.) Post ramp, these perturbations obey

$$\begin{aligned} \frac{d\delta s_n}{dt} &= \left[-\frac{G}{\eta} \mathbf{S}(s_0) \mathbf{p} - \frac{1}{\tau} \partial_s \mathbf{R} \Big|_{s_0} \right] \cdot \delta s_n \\ &\simeq -\frac{G}{\eta} \mathbf{S}(s_0) \mathbf{p} \cdot \delta s_n. \end{aligned} \quad (32)$$

The approximation on the second line is valid for small values of the Newtonian viscosity compared with the zero shear polymer viscosity, $\eta \ll G\tau$, which is a good approximation in most complex fluids. Because the base state s_0 is continuous across the end of the ramp, it follows that *immediately* post-ramp the perturbations obey

$$\frac{d\delta s_n}{dt} \Big|_{t^{*+}} = -\frac{G}{\eta} \mathbf{S}(s_0^*) \mathbf{p} \cdot \delta s_n. \quad (33)$$

Combining Eqn. 30 for the dynamics of the base state immediately before the ramp ends with Eqn. 33 for the dynamics of the heterogeneous perturbations immediately post-ramp, we get

$$\frac{\delta s_n}{dt} \Big|_{t^{*+}} = -\frac{G}{\eta} \frac{ds_0}{d\gamma_0} \Big|_{t^{*-}} \mathbf{p} \cdot \delta s_n \quad (34)$$

Projecting out the first component of this equation using the operator \mathbf{p} , and appealing to the linearity of the force balance condition (26), it is easy to show finally that shear rate perturbations obey, immediately post-ramp:

$$\frac{\delta \dot{\gamma}_n}{dt} \Big|_{t^{*+}} = -\frac{1}{\eta} \frac{\partial \Sigma_0}{\partial \gamma_0} \Big|_{t^{*-}} \delta \dot{\gamma}_n. \quad (35)$$

This important result tells us that, immediately after a strain ramp has ended, an initially homogeneous flow state will be linearly unstable to the onset of shear banding if the shear stress had been decreasing in strain immediately before the ramp ended:

$$\frac{\partial \Sigma_0}{\partial \gamma_0} \Big|_{t^{*-}} < 0. \quad (36)$$

This is consistent with the original insight of Marrucci and Grizzuti⁵⁸ in the context of the DE model.

As usual, this criterion is expressed as a condition on the shape of the stress signal of an underlying base state

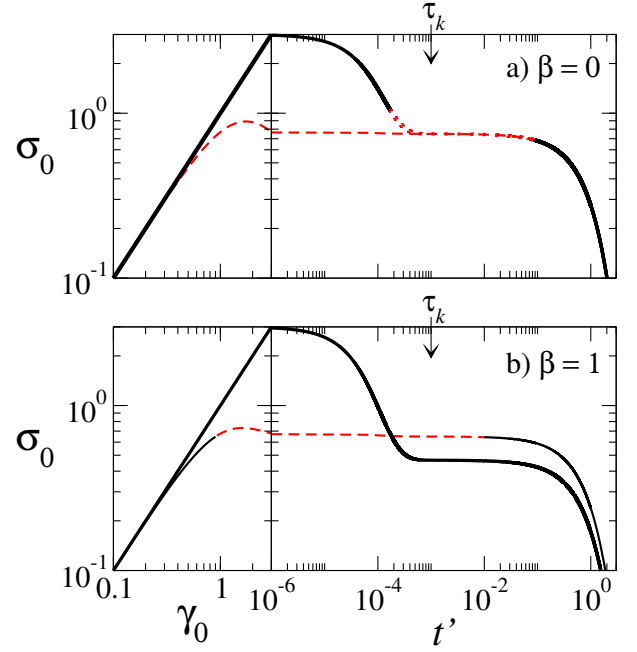


FIG. 9. Viscoelastic contribution to the shear stress in the RP model during (*vs.* γ_0) and after (*vs.* t') a strain ramp of amplitude $\gamma^* = 3$, with homogeneity enforced. (a) $\beta = 0$ (no CCR), (b) $\beta = 1$ (CCR active). Dotted/dashed lines denote linearly unstable regions ($\omega > 0$). Upper curve at the end of each ramp is for a ramp rate $\dot{\gamma}_{0,s}$ in the regime of chain stretch. Lower curve at the end of each ramp is for a ramp rate $\dot{\gamma}_{0,n} = 500$ in the non-stretch regime. Parameters: $\tau_R = 10^{-4}$, $\eta = 10^{-5}$, $\tau_k = 10\tau_R$.

of homogeneous flow response to the applied deformation. By definition, this base state stress signal equals the globally measured one at least until any significant banding takes place. Accordingly (36) can also be applied directly to the experimentally measured stress signal. (This assumes that no appreciable banding developed during the ramp itself, which is a good assumption for the fast finite-amplitude ramps of interest here: even if the flow technically becomes linearly unstable to banding during the ramp, there is insufficient time for heterogeneity to develop.)

B. Numerical results: RP model

In the previous section above we developed a criterion for linear instability, immediately following a rapid strain ramp, to the onset of shear banding post-ramp. This criterion is expressed as a condition on the shape of the stress signal of an underlying base state of homogeneous flow response to the applied deformation, immediately as the ramp ends.

In the next subsection below we shall present numerical results for this base state signal throughout the full duration of its evolution, both during and after ramp. We also present numerical results for any regions of lin-

ear stability (negative eigenvalues) or instability (positive eigenvalue) during this entire evolution. Recall that our analytically derived criterion (36) above strictly only applies immediately post-ramp. In the second subsection below we present the results of our spatially aware nonlinear simulations of the shear bands that arise as the result of any regimes of instability.

1. Base state and linear instability

Numerical results for the evolution of the base state stress signal, both during and after the ramp, are shown for the RP model in Fig. 9. (Here we have subtracted from Σ_0 the trivial contribution $\eta\dot{\gamma}_0$ from the Newtonian solvent to leave the viscoelastic contribution σ_0 only.) For clarity it is plotted as a function of strain during the ramp, and of time afterwards. Regimes of linear instability to shear banding, determined by numerically calculating the time-dependent eigenvalue of the linearised equations discussed above, are shown as dotted and dashed lines. Consistent with our criterion (36) above, ramps that end with declining stress leave the system unstable immediately post-ramp.

With this figure in mind, we discuss now in more detail separately ramps that are slower and faster than the rate of stretch relaxation τ_R^{-1} . (As noted above, in each case the ramp is faster than the inverse terminal relaxation time, $\dot{\gamma}_0\tau_d \gg 1$.)

Consider first a ‘slow’ ramp at a rate $\dot{\gamma}_{0,n}$ for which $\dot{\gamma}_{0,n}\tau_R \ll 1$. For such a ramp, no appreciable chain stretch develops: subscript ‘n’ denotes nonstretching. The ramp is still nonetheless in the fast flow regime $\dot{\gamma}\tau_d \gg 1$ of the non-stretching version of the model specified by Eqns. 11 above. The corresponding mechanical response during the ramp can then be computed by integrating only the terms prefactored by $\dot{\gamma}$ in Eqns. 11: it is effectively that of a nonlinear elastic solid with a stress signal that depends only on strain $\Sigma_0 = \Sigma_0(\gamma_0)$, independent of strain rate. Numerical results for this are shown by the lower of the two curves (during the ramp) in each panel of Fig. 9. It displays an overshoot at an amplitude $\gamma_0 \sim 1.7$. The system is therefore left unstable immediately post-ramp, as indicated by the red dashed lines, consistent with our criterion (36).

Post-ramp the base state stress signal shows mono-exponential decay on the single reptation timescale τ_d of tube reorientation, as the system relaxes back to equilibrium. Allied to this, the eigenvalue of the stability analysis shows monotonic decay from its initial value towards a final value $-(\frac{1}{\tau_d} + \frac{1}{\eta})$ which, being negative, indicates stability of the final homogeneous equilibrium state, as expected. Any system left linearly stable immediately post-ramp, by a ramp of amplitude $\gamma_0 < 1.7$, will therefore remain stable for all subsequent times and exhibit no banding. (This case is not shown in the figure.) In contrast, a system that is left linearly unstable immediately post-ramp by a ramp of amplitude $\gamma_0 > 1.7$, re-

turns finally to a stable homogeneous state. (See again the lower curve at the end of the ramp in each panel of Fig. 9.) However shear bands do transiently form during the relaxation process, as we shall discuss in more detail in the next subsection below.

Having discussed ‘slow’ ramps with $\dot{\gamma}_{0,n}\tau_R \ll 1$, we now address ‘fast’ ramps of typical rate $\dot{\gamma}_{0,s}$ such that $\dot{\gamma}_{0,s}\tau_R \gg 1$. Here appreciable chain stretch develops during the ramp. (Subscript ‘s’ denotes stretching.) The associated mechanical response during the ramp then follows by integrating the terms in $\dot{\gamma}$ in the sRP model Eqns. 10. It again corresponds to that of an elastic solid, independent of strain rate in this limit. Indeed because of the simple linear structure of the $\dot{\gamma}$ terms in the sRP model, we now have a monotonically increasing relation $\sigma_0 = G\gamma_0$. The system is therefore left linearly stable against banding immediately post-ramp, as seen in the upper curve at the end of the ramp in each panel of Fig. 9, and consistent with our analytical criterion (36).

However it is important to recall that our analytically derived criterion (36) applies only *immediately* post-ramp and does not prescribe the system’s stability properties throughout the full duration of its relaxation back to equilibrium post-ramp. As seen in the upper curve (at the end of each ramp) in each panel of Fig. 9, this relaxation after a ramp of rate $\dot{\gamma}_{0,s} \gg 1$ shows a double exponential form: first as chain stretch relaxes on the fast timescale τ_R , and subsequently as tube reorientation takes place on the much slower reptation timescale τ_d .

Subfigures (a) and (b) respectively address a system without ($\beta = 0$) and with ($\beta = 1$) the mechanism convective constraint release (CCR) active. Immediately striking is the fact that, without CCR (subfigure a) the first part of the stress relaxation on the fast timescale of stretch relaxation τ_R , returns the stress to a value equal to that which would have been generated by a ramp of equivalent amplitude in the slower non-stretching limit: the upper curve in subfigure (a) rejoins the lower one on an intermediate plateau around the time $\tau_k = 10\tau_R$, before both finally follow the same decay on the terminal timescale τ_d . Denoting by $\sigma(t' = \tau_k, \dot{\gamma}_0, \gamma_0)$ the stress on this intermediate plateau, then, for a ramp of amplitude γ_0 we have

$$\sigma(\tau_k, \dot{\gamma}_{0,s}, \gamma_0) = \sigma(\tau_k, \dot{\gamma}_{0,n}, \gamma_0) \quad \text{for } \beta = 0. \quad (37)$$

Once this intermediate plateau has been attained, the stability properties of the two curves in Fig. 9a) coincide. Following a fast ramp of rate $\dot{\gamma}_{0,s}$ and amplitude $\gamma_0 > 1.7$, therefore, we predict a *delayed* banding instability that sets in a time $O(\tau_R)$ post-ramp, even though no stress overshoot occurred during the ramp itself. This will be confirmed by our spatially aware simulation showing shear banding in the next subsection below. It is consistent with experimental results that show delayed shear banding setting in on a timescale $O(\tau_R)$ post-ramp^{9,16}.

In contrast, with CCR active ($\beta \neq 0$) the stress remaining after the initial part of the stress decay on the fast timescale τ_R is significantly lower than that which would

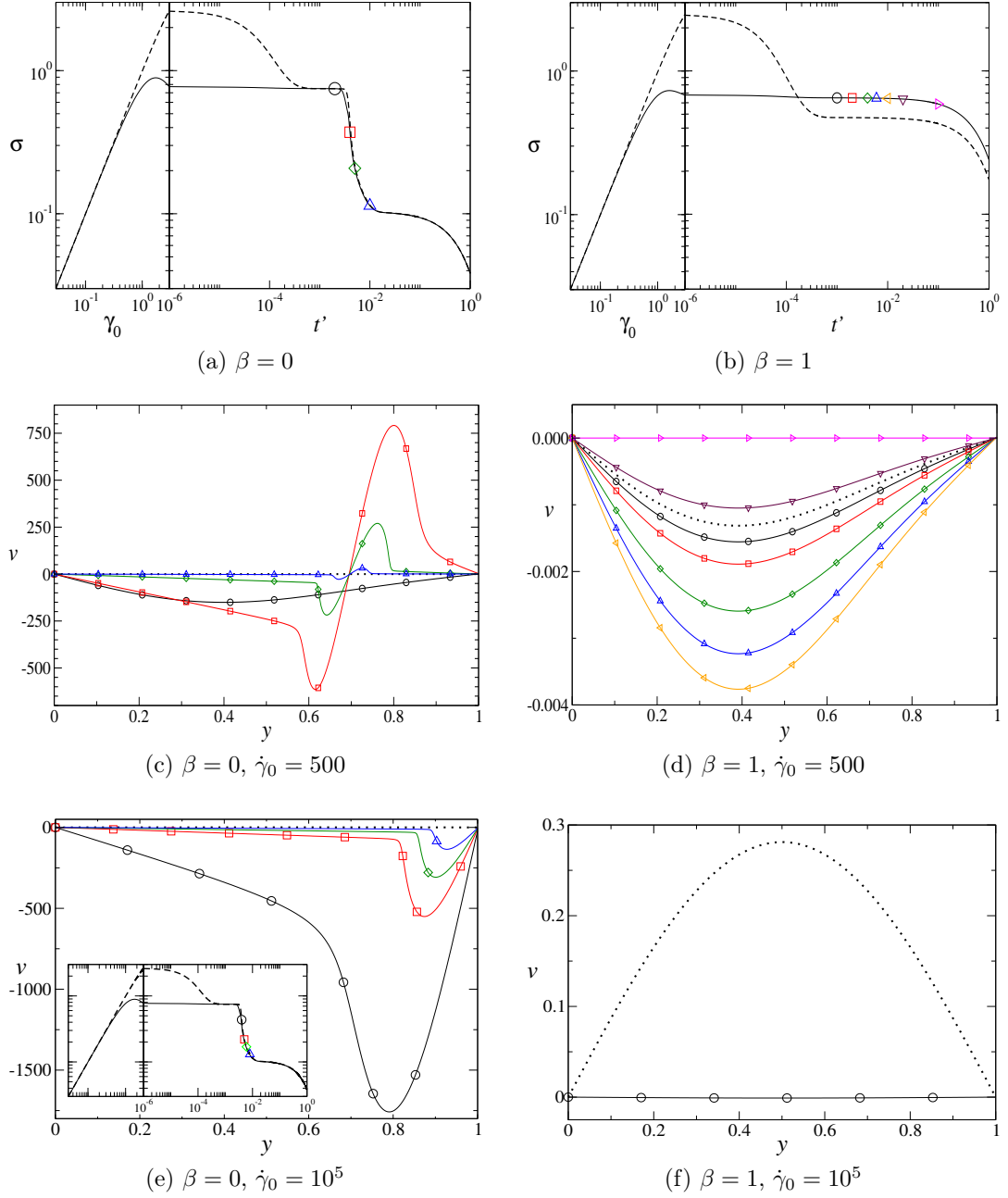


FIG. 10. Strain ramp in the RP model. (a) Shear stress during (*vs.* γ_0) and after (*vs.* t') a ramp of amplitude $\gamma^* = 3$, with CCR inactive, $\beta = 0$. The dashed line is for a ramp of fast rate $\dot{\gamma}_{0,s} = 10^5$ in the chain stretching regime; the solid line is for a ramp of rate $\dot{\gamma}_{0,n} = 500$ in the non-stretching regime. (b) Corresponding curves with CCR active, $\beta = 1$. (c) and (d) show velocity profiles during stress relaxation at times corresponding to symbols in (a) and (b) respectively, in both cases following a ramp of rate in the non-stretching regime $\dot{\gamma}_{0,n} = 500$. Corresponding figures (e) and (f) are for a ramp of fast rate $\dot{\gamma}_{0,s} = 10^5$ in the stretching regime. Profiles are shown at times corresponding to symbols in the inset for (e), and at times corresponding to symbols in (b) for (f). The normalised velocity heterogeneity $v_0(y) = v(y) - \dot{\gamma}_0 y$ immediately before the end of the ramp at $t = t^{*-}$ is shown as a thick dotted line. Model parameters $\tau_R = 10^{-4}$, $\eta = 10^{-5}$. Initial noise magnitude: $q = 5 \times 10^{-4}$.

have been generated by a ramp of corresponding amplitude in the slower, non-stretching regime: the intermediate plateau values do not coincide in Fig. 9 (b). Indeed, for large enough β this initial fast relaxation is sufficient to ensure that the system remains stable against the for-

mation of bands throughout the full duration of its return to equilibrium, as seen in Fig. 9(b). We therefore conclude that in order to observe shear banding after a ramp in the chain stretching regime, the value of the CCR parameter β should be small $\beta \sim 0$.

These differences in the system's relaxation properties with and without CCR can be explained as follows. Without CCR ($\beta = 0$), the mechanisms of chain stretch relaxation and tube orientation relaxation are decoupled and occur independently of each other. The residual stress remaining after chain stretch has relaxed following a 'fast' ramp of rate $\dot{\gamma}_{0,s}$ is therefore equal to the stress that would have resulted from a ramp of the same amplitude but rate $\dot{\gamma}_{0,n}$ during which no chain stretch arose in the first place. In contrast, with CCR ($\beta \neq 0$) the relaxation of chain stretch also brings significant relaxation in the orientation of tube segments, because a proportion of the entanglements forming the tube of constraints on a test chain are lost upon stretch relaxation. The stress relaxation is thereby accelerated for times $t' < \tau_R$ compared with the non-CCR case.

2. Nonlinear, spatially aware simulations

So far, we have discussed the evolution of the base state stress during and after a strain ramp, and its associated time-dependent linear stability properties. We now perform nonlinear simulations to investigate the shear bands that form as a result of any regime of linear instability.

As can be seen in Fig. 10 the results are consistent with our linear instability predictions of Fig. 9. Subfigures (c) and (d) show that shear rate perturbations grow as soon as a ramp of rate $\dot{\gamma}_{0,n}$ and amplitude $\gamma_0 > 1.7$ ends. For example, appreciable heterogeneity has already developed by the time indicated by the circle in (a). In contrast, subfigures (e) and (f) show that after a 'fast' ramp of rate $\dot{\gamma}_{0,s}$ and amplitude $\gamma_0 > 1.7$, the system shows onset of shear rate heterogeneity only after a delay time $t' \sim \tau_k$, and only for systems in which CCR is sufficiently small $\beta \sim 0$ (subfigure e). With CCR active (subfigure f) any residual heterogeneity at the end of the ramp decays monotonically.

Fig. 10 (a) also demonstrates that shear rate heterogeneity of the large magnitude seen in this protocol can dramatically alter the stress relaxation function. As the local shear rate becomes extremely large, nonlinearities become important and result in a sudden and dramatic acceleration of stress relaxation compared with the base state signal of Fig. 9. This causes the second drop-off in stress in that subfigure. (Recall that the first drop-off after the fast ramp in contrast arose from chain stretch relaxation in the underlying base state.)

C. Comparison with experiment

We now discuss our results in relation to experimental observations of shear banding following the imposition of a fast strain ramp in polymeric fluids. In doing so, we recall that shear banding is often described as 'macroscopic motions' in the context of this protocol.

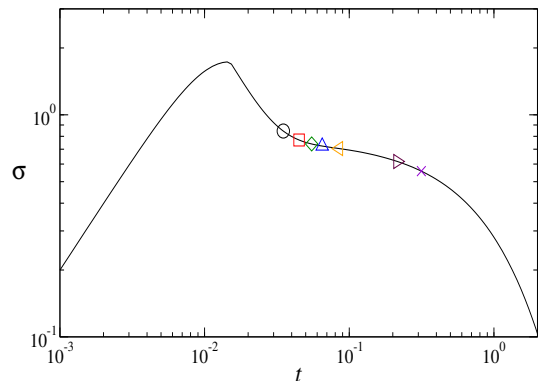


FIG. 11. Viscoelastic stress during and after a strain ramp of amplitude $\gamma_0 = 3$ and rate $\dot{\gamma}_0 = 200$, time of shear cessation: $t^* = 0.015$. Here $\tau_R = 10^{-2}$, $\eta = 10^{-5}$, $\beta = 0$, and initial noise magnitude: $q = 10^{-2}$.

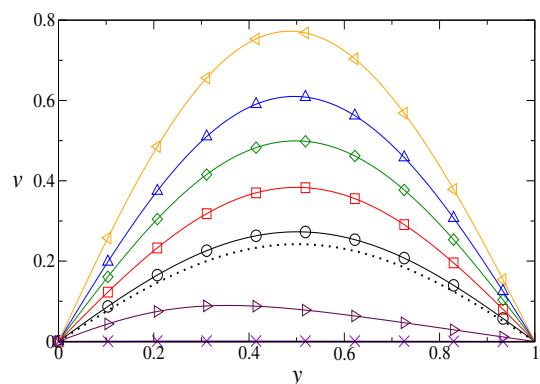


FIG. 12. Snapshots of the velocity profile during stress relaxation after a ramp shown in Figure 11, at times corresponding to symbols in that figure. Dotted line: snapshot of the normalised velocity profile $v_0(y) = v(y) - \dot{\gamma}_0 y$ at time $t = t^*$.

For strain ramps that terminate in a regime of declining stress versus strain, macroscopic motions accompanied by a dramatic drop in the stress signal were reported to develop quickly post-ramp in Refs.^{12,13}. This is consistent with our analytical criterion (36), and also with our numerics in Figs. 10(c) and (d).

For strain ramps of amplitudes $\gamma_0 \gtrsim 1.5$ that show no stress overshoot during the ramp, delayed macroscopic motions have been reported post-ramp in polymer melts^{13,16} and solutions⁹. These onset after a time $t' = O(\tau_R)$ and are concurrent with a sudden drop in the stress signal. These observations are consistent with the stress response and associated transient shear banding in the RP model for $\beta \sim 0$ following a strain ramp of rate $\dot{\gamma}_{0,s}$ and amplitude $\gamma_0 \gtrsim 1.7$: recall Fig. 10(e).

Experimental reports of similar macroscopic motions but without the accompanying dramatic drop in the stress signal post-ramp are also widespread^{16,28,49,72,74,88}. Qualitatively similar behaviour can be uncovered in the RP model by decreasing the entanglement number Z to give less well separated relaxation timescales τ_d, τ_R . This

decreases the maximal degree of banding observed post-ramp to a sufficient extent that the global stress signal no longer differs significantly from that of the homogeneous constrained system. An example of such behaviour is shown in Figs. 11 and 12. The stress signal now shows a single dropoff associated with chain stretch relaxation, but lacks a second dropoff associated with the nonlinear effects of banding.

Indeed, our numerical runs in Figs. 9 and 10 assumed an entanglement number $Z = 3300$ larger than is the case experimentally. We set this number deliberately to ensure a clean separation of timescales $\tau_d = 10^4 \tau_R$, thereby allowing a clear pedagogical discussion of the relative effects of the relaxation of chain stretch and the relaxation of tube orientation post-ramp.

In practice, however, polymer melts with $Z \gtrsim 100$, and DNA or wormlike micelles with $Z \gtrsim 150$, usually suffer edge fracture so that reliable results are difficult to obtain. The separation of time scales in experiment is therefore more typically $\tau_d/\tau_R \sim 150 - 500$. Upon repeating our simulations for these more realistic values of τ_d/τ_R , and for less severe ramp rates $\dot{\gamma}_{0,s}$, we find, reassuringly, that the qualitative features described above still obtain (provided $\tau_d/\tau_R \gtrsim 10$ and $\dot{\gamma}_{0,s} > \tau_R^{-1}$). See Figs. 11 and 12. We do not attempt to reproduce specific experimental results by matching the relaxation times or ramp rates in detail in this work, because studies elsewhere have done so^{6,7}.

Finally, we comment on our numerical findings in relation to the A, B, C classification system discussed in Sec. II above. As seen towards the right hand side of Figs. 10, the development of very large local shear rates post-ramp is closely associated with a stress relaxation that is accelerated compared with that which would be predicted by a calculation in which homogeneity is imposed by assumption. This can result in a significant decrease in the damping function compared with that predicted by any homogeneous calculation and so to type C behaviour. Conversely, for systems in which the macroscopic motions that develop are more modest (even if still observable experimentally), the stress relaxation function agrees well with that of a calculation in which homogeneity is assumed, leading to a damping function of type A.

Furthermore, a decreasing separation of relaxation times τ_d/τ_R (decreasing entanglement number Z) causes the maximal degree of banding to decrease and so could lead correspondingly to a progression from type C to type A behaviour. This is consistent with reports that type C behaviour is most common in very well entangled polymers, while type A behaviour occurs most often for moderately entangled polymers^{64,85}. We conclude that the RP model is capable of exhibiting both types A and C behaviour, with a progression between the two consistent with that seen experimentally. To the best of our knowledge, the RP model is unable to show the less commonly reported type B behaviour of very weakly entangled materials^{64,85}. Indeed, the RP model is in any case not aimed at describing these systems.

We note finally that the Giesekus model has a linear stress-strain relation in a fast strain ramp protocol: $\Sigma \sim G\gamma$. It therefore predicts linear stability against shear banding immediately after a fast strain ramp, according to (36). Furthermore this model contains only one relaxation time. Accordingly it is unlikely to capture the rich experimental phenomenology just discussed for this protocol, and we do not discuss it further here.

VII. RESULTS: SHEAR STARTUP

We consider finally the shear startup protocol, in which a previously well rested sample is subject to shearing at a constant rate $\dot{\gamma}_0$ for all times $t > 0$, giving a strain $\gamma_0 = \dot{\gamma}_0 t$. We first derive an analytical criterion for the onset of banding in this protocol, before presenting numerical results that support it.

A. Criterion for instability in shear startup

In a shear startup experiment, the most commonly reported rheological response function is that of the startup stress as a function of time t , or equivalently as a function of strain $\gamma_0 = \dot{\gamma}_0 t$, for the given applied strain rate $\dot{\gamma}_0$. When plotted as a function of accumulated strain γ_0 for a collection of startup runs, each performed at a constant value of the strain rate $\dot{\gamma}_0$, this gives us a two-dimensional function $\Sigma_0(\gamma_0, \dot{\gamma}_0)$.

In the context of shear banding, a familiar thought-experiment is to consider an (artificial) situation in which a startup flow is constrained to remain homogeneous until the system attains a stationary state in the limit $\gamma_0 \rightarrow \infty$. In this limit, the total accumulated strain becomes irrelevant and the stress depends only on strain rate: $\Sigma_0 = \Sigma_0(\dot{\gamma}_0)$. The criterion for shear banding (with the constraint now removed) is well known in this limit: that the underlying constitutive curve of stress as a function of strain rate has negative slope, $d\Sigma_0/d\dot{\gamma}_0 < 0$.

Our aim here is to generalise this result, which is valid only for a stationary homogeneous base state in the limit $\gamma_0 \rightarrow \infty$, to finite strains γ_0 and times t , in order to predict at what stage during startup banding first sets in. As we shall show, the onset of banding is closely associated with the time (or equivalent strain) of any overshoot in the stress startup signal $\Sigma_0(\gamma_0)$, for a given applied strain rate $\dot{\gamma}_0$. Clearly this implies an onset criterion $d\Sigma_0/d\gamma_0 < 0$, which is indeed a very useful rule of thumb to apply to experimental data. However we show below that it is in fact modified slightly, leading to onset a little before overshoot.

Besides predicting the time at which bands first start to form in any experiment for which the eventual steady state is banded, $d\Sigma_0/d\dot{\gamma}_0 < 0$, an important further outcome of what follows will be to predict the transient appearance of shear bands, again associated with a startup overshoot and subsequently declining stress $d\Sigma_0/d\gamma_0 < 0$,

even in systems for which the underlying constitutive curve is monotonic $d\Sigma_0/d\dot{\gamma}_0 > 0$ and the steady state unbanded.

As ever, our strategy will be to consider an underlying base state of initially homogeneous flow response, and the dynamics of small heterogeneous perturbations about it. Our criterion for the growth of these perturbations, *i.e.*, for the onset of banding, will be expressed in terms of the partial derivatives of the base state stress signal $\Sigma_0(\gamma_0, \dot{\gamma}_0)$ with respect to γ_0 and $\dot{\gamma}_0$.

In many places below we shall graphically present results in the plane of γ_0 and $\dot{\gamma}_0$. To interpret data presented in this way, it is useful to keep in mind that a vertical cut up this plane at its far right hand side $\gamma_0 \rightarrow \infty$ corresponds to the system's steady state properties as a function of strain rate $\dot{\gamma}_0$. A horizontal cut corresponds to the system's startup behaviour as a function of accumulated strain γ_0 , in a single startup run performed at a fixed value of the strain rate $\dot{\gamma}_0$.

As noted in the context of the other protocols above, because the base state signal corresponds to the experimentally measured one at least until appreciable banding develops, the criterion that we develop can be applied directly to experimentally measured stress startup data.

To start, then, we consider the properties of an underlying base state of initially homogeneous flow response to an imposed shear startup deformation. Were the flow to remain homogeneous through to the stationary limit $\gamma_0 \rightarrow \infty$, the condition for banding instability would then be that the stationary constitutive curve of stress as a function of strain rate has a region of negative slope $d\Sigma_0/d\dot{\gamma}_0 < 0$, as noted above. In practice, however, the flow generally becomes unstable to banding before this stationary limit is attained. As a first step to generalising our onset criterion to finite strains during startup, we define a fixed-strain constitutive curve:

$$\Sigma_0(\dot{\gamma}_0)|_{\gamma_0=\text{const.}} = G W_{xy0}(\dot{\gamma}_0)|_{\gamma_0=\text{const.}} + \eta \dot{\gamma}_0. \quad (38)$$

Experimentally, such a curve would be constructed by performing a series of startup runs at different shear rates and plotting the shear stress, grabbed at the same fixed strain γ_0 in each run, as a function of the applied shear rate.

We then consider the derivative of this fixed-strain constitutive curve with respect to shear rate:

$$\partial_{\dot{\gamma}_0} \Sigma_0|_{\gamma_0} = G \partial_{\dot{\gamma}_0} W_{xy0}|_{\gamma_0} + \eta. \quad (39)$$

This clearly reduces to the slope of the underlying steady state constitutive curve $d\Sigma_0/d\dot{\gamma}_0$ in the limit $\gamma_0 \rightarrow \infty$, and more generally is the finite-strain analogue of it.

To proceed further, we need an expression for $\partial_{\dot{\gamma}_0} W_{xy0}|_{\gamma_0}$. To obtain this we return to Eqn. 14, divided across by strain rate:

$$\partial_{\dot{\gamma}_0} \mathbf{s}_0|_{\dot{\gamma}_0} = \frac{1}{\dot{\gamma}_0} \mathbf{Q}(\mathbf{s}_0, \dot{\gamma}_0). \quad (40)$$

(We again neglect diffusive terms, which are small for the most unstable mode in the linear regime.) Differentiating

this with respect to strain rate gives

$$\partial_{\dot{\gamma}_0} \partial_{\dot{\gamma}_0} \mathbf{s}_0 = -\frac{1}{\dot{\gamma}_0} \partial_{\dot{\gamma}_0} \mathbf{s}_0|_{\dot{\gamma}_0} + \frac{1}{\dot{\gamma}_0} \mathbf{M} \cdot \partial_{\dot{\gamma}_0} \mathbf{s}_0|_{\dot{\gamma}_0} + \frac{1}{\dot{\gamma}_0} \mathbf{q}, \quad (41)$$

in which $\mathbf{M} = \partial_{\mathbf{s}} \mathbf{Q}|_{\mathbf{s}_0, \dot{\gamma}_0}$ and $\mathbf{q} = \partial_{\dot{\gamma}} \mathbf{Q}|_{\mathbf{s}_0, \dot{\gamma}_0}$, as previously. Multiplying by $\dot{\gamma}_0 \mathbf{M}^{-1}$ and rearranging we have

$$\partial_{\dot{\gamma}_0} \mathbf{s}_0|_{\dot{\gamma}_0} = \mathbf{M}^{-1} \cdot (\partial_{\dot{\gamma}_0} \mathbf{s}_0|_{\dot{\gamma}_0} - \mathbf{q} + \dot{\gamma}_0 \partial_{\dot{\gamma}_0} \partial_{\dot{\gamma}_0} \mathbf{s}_0). \quad (42)$$

Using \mathbf{p} to project out the first component gives

$$\partial_{\dot{\gamma}_0} W_{xy0}|_{\dot{\gamma}_0} = \mathbf{p} \cdot \mathbf{M}^{-1} \cdot (\partial_{\dot{\gamma}_0} \mathbf{s}_0|_{\dot{\gamma}_0} - \mathbf{q} + \dot{\gamma}_0 \partial_{\dot{\gamma}_0} \partial_{\dot{\gamma}_0} \mathbf{s}_0), \quad (43)$$

which, substituted into Eqn. 39, gives finally an expression

$$\partial_{\dot{\gamma}_0} \Sigma_0|_{\dot{\gamma}_0} = G \mathbf{p} \cdot \mathbf{M}^{-1} (\partial_{\dot{\gamma}_0} \mathbf{s}_0|_{\dot{\gamma}_0} - \mathbf{q} + \dot{\gamma}_0 \partial_{\dot{\gamma}_0} \partial_{\dot{\gamma}_0} \mathbf{s}_0) + \eta \quad (44)$$

for the derivative with respect to shear rate of the fixed-strain constitutive curve of the underlying homogeneous base state. We shall return to this expression in a few lines below.

We now turn to consider the dynamics of any heterogeneous perturbations to the homogeneous base state just discussed. Recalling Eqns. 18 and 19, we have

$$\partial_t \delta \mathbf{s}_n = \left(\mathbf{M} - \frac{G}{\eta} \mathbf{q} \mathbf{p} \right) \cdot \delta \mathbf{s}_n. \quad (45)$$

The criterion for this system of linear equations to have a positive eigenvalue, which signifies onset of instability to the growth of shear banding perturbations at any time, is

$$(-1)^D \left| \mathbf{M} - \frac{G}{\eta} \mathbf{q} \mathbf{p} \right| > 0, \quad (46)$$

where D is the dimensionality of \mathbf{M} . (We neglect the possibility of the emergence of two complex conjugate eigenvalues of positive real part - a Hopf bifurcation - because we have never seen this in practice in our numerics.) This corresponds exactly to

$$(-1)^D |\mathbf{M}| \left(1 - \frac{G}{\eta} \mathbf{p} \cdot \mathbf{M}^{-1} \cdot \mathbf{q} \right) > 0. \quad (47)$$

Using the fact that $(-1)^D |\mathbf{M}| < 0$ (which follows from noting that the base state must be stable with respect to *homogeneous* perturbations at fixed $\dot{\gamma}_0$), this further corresponds exactly to

$$\eta - G \mathbf{p} \cdot \mathbf{M}^{-1} \cdot \mathbf{q} < 0. \quad (48)$$

Combining this with equation (44) above for the base state, we find finally an exact criterion for the onset of a linear instability to shear banding during startup:

$$\partial_{\dot{\gamma}_0} \Sigma_0|_{\dot{\gamma}_0} - G \mathbf{p} \cdot \mathbf{M}^{-1} \cdot (\partial_{\dot{\gamma}_0} \mathbf{s}_0|_{\dot{\gamma}_0} + \dot{\gamma}_0 \partial_{\dot{\gamma}_0} \partial_{\dot{\gamma}_0} \mathbf{s}_0) < 0. \quad (49)$$

In raw form, this criterion appears cumbersome and somewhat removed from conveniently measurable experimental quantities. However its overall structure is physically transparent. The first term is a derivative of the

base state stress with respect to strain rate. The second term is a derivative of the base state with respect to strain. The third is a cross term, containing derivatives with respect to both. To illuminate its physical content, therefore, we start by discussing two distinct and physically important limits in which the first and second terms separately dominate.

Consider first an (artificial) situation in which a homogeneous startup flow proceeds through to a stationary state in the limit of large strain $\gamma_0 \rightarrow \infty$, without banding en route. In this limit, derivatives with respect to strain ∂_γ vanish from (49) and we recover the familiar, and much simpler, criterion for banding in steady state already discussed above

$$\partial_{\dot{\gamma}} \Sigma_0 |_{\gamma_0 \rightarrow \infty} < 0. \quad (50)$$

This criterion also applies (less artificially) to the onset of a linear instability to shear banding during an experiment in which the strain rate $\dot{\gamma}_0$ is slowly swept upwards from zero. Because the material is flowing in a liquid-like way in this limit, we term this a ‘viscous instability’ for convenient nomenclature in what follows.

Consider conversely a single startup run performed in the limit of a very fast flow $\dot{\gamma}_0 \rightarrow \infty$. In this regime many viscoelastic materials behave essentially as elastic solids, with the stress startup function converging to a limiting curve $\Sigma_0(\gamma_0)$ from which any dependence on shear rate is lost, $\partial_{\dot{\gamma}} \rightarrow 0$. The full criterion (49) then reduces to

$$-G \mathbf{p} \cdot \mathbf{M}^{-1} \cdot \partial_{\gamma_0} \mathbf{s} |_{\dot{\gamma}_0} < 0. \quad (51)$$

Because in this limit the material responds essentially as an elastic solid, we term this an ‘elastic instability’ for convenient nomenclature in what follows.

Although simpler than (49), (51) is still not expressed in terms of quantities that are easily measured experimentally. However further simplification is possible in the case of only two dynamical variables $D = 2$, for example in flow regimes in which the dynamics is dominated by the shear stress and only one component of normal stress difference. In this case (51) further reduces to

$$-\frac{1}{\dot{\gamma}_0^2} \text{tr} \mathbf{M} \partial_{\gamma_0} \Sigma_0 |_{\dot{\gamma}_0} + \frac{1}{\dot{\gamma}_0} \partial_{\gamma_0}^2 \Sigma_0 |_{\dot{\gamma}_0} < 0 \quad \text{with} \quad \text{tr} \mathbf{M} < 0. \quad (52)$$

Taken alone, the first term of this expression predicts onset of banding immediately after any overshoot in the stress as a function of strain during startup. The second term modulates this result slightly, allowing onset slightly before overshoot, once the stress starts to curve downwards. This prediction is consistent with numerous experimental observations of time-dependent shear banding associated with stress overshoot during startup: in soft glassy materials^{23,24} and entangled polymer melts and solutions^{15,41,73,75,84}, and also in simulation studies^{3-5,19,57,60,90}.

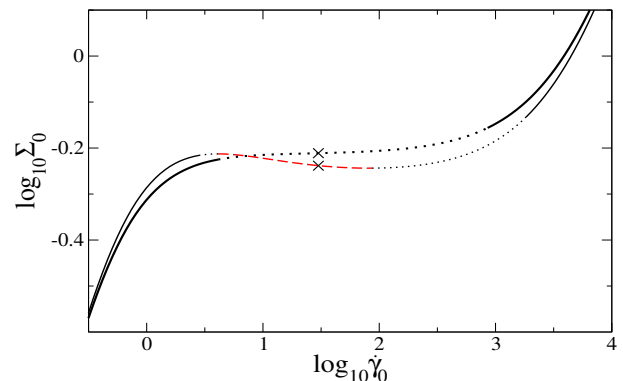


FIG. 13. Constitutive curves of the nRP model for $\beta = 0.4, 1$ (bottom to top on the right) and $\eta = 10^{-4}$. Dashed: linearly unstable at steady state. Dotted: *transiently* linearly unstable before the steady state is reached. Crosses denote shear rate $\dot{\gamma} = 30$ for which time-dependent shear startup behaviour is explored in Fig. 14.

B. Numerical results: rolie-poly model

In this section, we present our numerical results for shear startup in the RP model. We consider first the limit in which polymer chain stretch is negligible, $\dot{\gamma}_0 \tau_R \ll 1$, before commenting on the effects of stretch.

The behaviour of the rolie-poly model in startup has been studied previously numerically in Refs.^{2,3}. One of our aims in what follows is to understand the phenomena reported in that work, some of which we must necessarily reproduce in our numerics here, in the context of the general analytical criterion developed above.

1. Nonstretching rolie-poly model

Depending on the values of the model parameters β, η , the underlying constitutive curve of the non-stretch rolie-poly (nRP) model can either be monotonic or non-monotonic. A representative example of each case is shown in Fig. 13.

We consider first the non-monotonic case, for a shear rate indicated by the cross in the negatively sloping regime $d\Sigma_0/d\dot{\gamma}_0 < 0$. The model’s shear startup behaviour at this imposed shear rate is explored in the bottom row of Fig. 14. The velocity profile shown by the thick dashed line in the bottom right subfigure shows that the steady flowing state is shear banded, consistent with a ‘viscous instability’ implied by the negative slope $d\Sigma_0/d\dot{\gamma}_0 < 0$ in the constitutive curve.

Also immediately obvious in Fig. 14 is the fact that bands first form rather early during the startup process, apparently triggered by an ‘elastic instability’ associated with the startup stress overshoot and subsequently declining stress $d\Sigma_0/d\dot{\gamma}_0 < 0$. When first formed these are much more pronounced than in steady state, as shown by the pronounced spike in the degree of banding $\Delta\dot{\gamma}$.

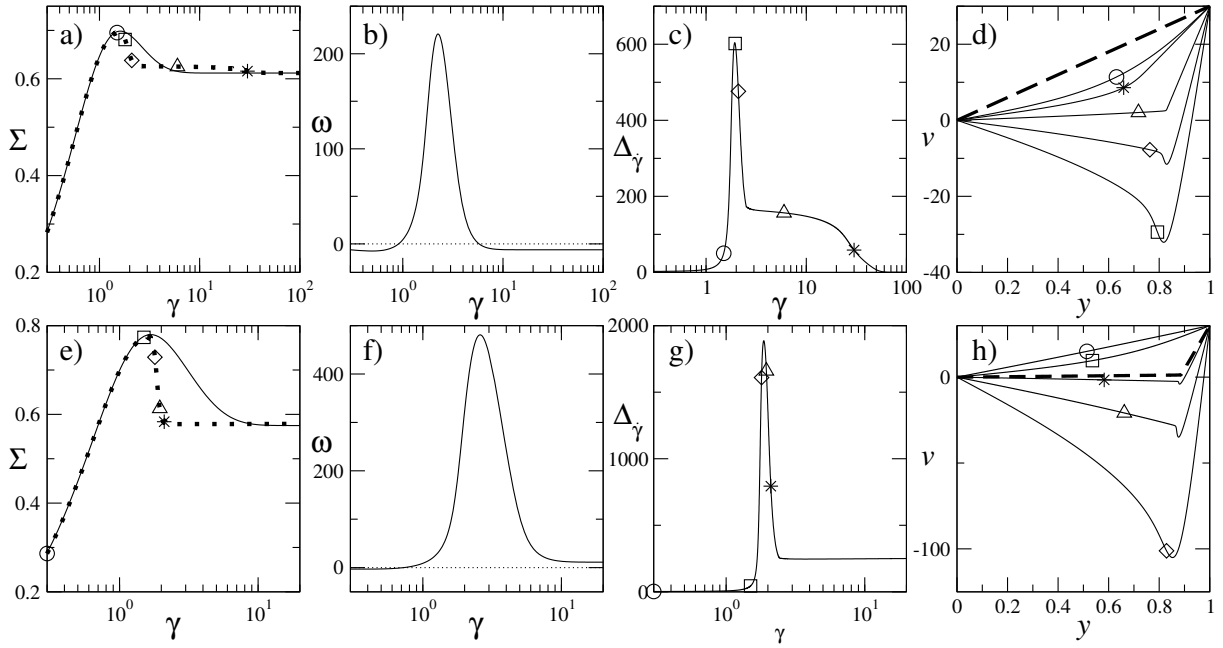


FIG. 14. Responses of the nRP model to an imposed shear rate $\bar{\dot{\gamma}} = 30$ for the case of a monotonic constitutive curve $\beta = 1$ (top row) and for the case of non-monotonic constitutive curve $\beta = 0.4$ (bottom row). (a, e) Shear stress response with homogeneity enforced (solid line) and with heterogeneity allowed (dotted line). (b, f) Linear stability analysis results for the real part of the eigenvalue that has the largest real part. (c, g). Degree of banding $\Delta\dot{\gamma} = \dot{\gamma}_{\max} - \dot{\gamma}_{\min}$ in full nonlinear simulations. (d, h) Snapshots of the velocity profile at strains corresponding to symbols in a/c, e/g). Steady state velocity profile is shown as a thick dashed line. $\eta = 10^{-4}$, $q = 0.1$.

Indeed this ‘elastic banding’ can be so pronounced as to precipitate negative local shear rates and negative local velocities at some regions across the cell, consistent with the material behaving as an elastic solid subject to a declining stress in this regime. Clearly, then, in shear startup an ‘elastic instability’ associated with stress overshoot can precede and be much more violent than any ‘viscous instability’ associated with steady state banding.

For shear rates shown by the dotted lines either side of the negatively sloping regime $d\Sigma_0/d\dot{\gamma}_0 < 0$ in Fig. 13, steady state ‘viscous instability’ is absent, but a pronounced ‘elastic instability’ can nonetheless still arise during startup. This leads to the formation of pronounced banding that persists only transiently, before decaying to leave homogeneous flow in steady state.

The model’s startup behaviour across a wide range of imposed shear rates $\dot{\gamma}_0$ is summarised in Fig. 16. In the left panel of this figure we show our linear stability criteria for the onset of banding in the full plane of $\dot{\gamma}_0, \gamma_0$. As noted above, horizontal cut across this plane corresponds to the fluid’s startup behaviour as a function of accumulated strain, at a single fixed value of the strain rate. A vertical cut at the far right hand side corresponds to the system’s steady state properties as a function of strain rate. We again use parameter values for β, η corresponding to the non-monotonic constitutive curve in Fig. 13. Accordingly, the startup run explored in the bottom row of Fig. 14 corresponds to horizontal slice through Fig. 15

at a fixed value of $\dot{\gamma}_0 = 30$.

In the left panel of Fig. 15, then, the black dotted line indicates the locus of strain values γ_0 for which the base state stress startup curves show a stress overshoot, with these curves measured across a range of closely spaced values of $\dot{\gamma}_0$. In other words, in any single startup run corresponding to a horizontal cut across this plane at a fixed $\dot{\gamma}_0$, the stress overshoot occurs at the strain indicated by this black dotted line. This line being vertical indicates that in fact the stress overshoot occurs at a fixed strain $\gamma \sim 1.7$ for all values of imposed shear rates.

The green solid line indicates the strain at which our criterion (52) for ‘elastic instability’ is first met in each horizontal startup slice. As can be seen this occurs just before overshoot in each run, due to the presence of the stress curvature terms in (52).

The dashed line encloses the region of viscous instability in which $\partial_{\dot{\gamma}}\Sigma_0|_{\gamma_0} < 0$, according to our criterion (50). At the far right hand side of the plane $\gamma_0 \rightarrow \infty$ this coincides with the region of negative slope in the underlying constitutive curve.

The large open circles enclose the region in which the full criterion (49) for linear instability to banding is met. We have cross-checked numerically that this indeed coincides with the region in which there exists a positive eigenvalue of the linearised equations, thereby verifying our analytical derivation of (49).

As can be seen, the full criterion (49) is very well represented by the much simpler elastic one (52) across a

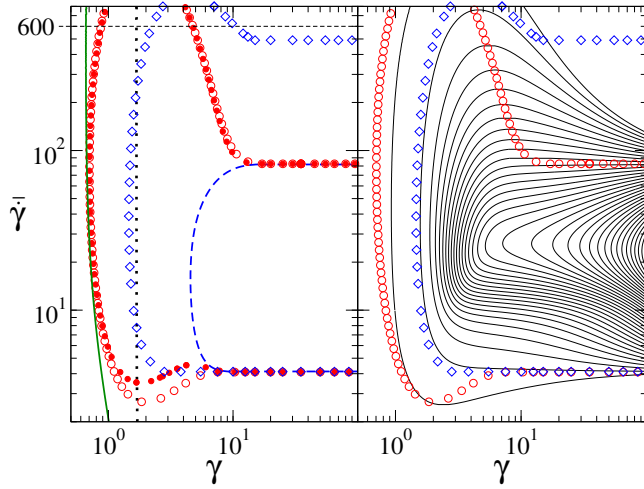


FIG. 15. Shear startup in the nRP model with a non-monotonic constitutive curve: $\beta = 0.4$, $\eta = 10^{-4}$. **Left panel.** Black dotted line: location of stress overshoot. Solid line: location of onset of ‘elastic instability’ (52). Dashed line encloses region of ‘viscous instability’ (50). Large open circles enclose region of linear instability according to full criterion (49). Small closed circles enclose region of linear instability according to the criterion with cross terms omitted (53). Diamonds enclose region in which significant shear banding is seen in our spatially aware nonlinear simulations. **Right panel.** Solid lines: contour lines of equal $|\delta\dot{\gamma}_{n=1}|/\dot{\gamma} = 10^M$ for integer M found by directly integrating the linearised Eqns. 45). (First contour: $M = -2$ and we show only contours $M \geq -2$.) Circles and diamonds as in left panel.

wide range of shear rates during the early stage of shear startup towards the left hand side of the $\dot{\gamma}_0, \gamma_0$ plane, and by the even simpler viscous one (50) at the far right hand side. This ability of the ‘elastic’ and ‘viscous’ criteria separately to capture the full criterion in these regimes leads us further to indicate by the small full circles the region in which a criterion formed simply by summing the elastic terms (52) and the viscous terms (50) is met:

$$\partial_{\dot{\gamma}_0} \Sigma_0 |_{\dot{\gamma}_0} - \frac{1}{\dot{\gamma}_0^2} \text{tr} \mathbf{M} \partial_{\dot{\gamma}_0} \Sigma_0 |_{\dot{\gamma}_0} + \frac{1}{\dot{\gamma}_0} \partial_{\dot{\gamma}_0}^2 \Sigma_0 |_{\dot{\gamma}_0} < 0. \quad (53)$$

This simple criterion performs well in capturing the region of instability across the full plane of $(\gamma_0, \dot{\gamma}_0)$, apart a small region at the bottom left.

As just described, the left panel of Fig. 15 concerns our criteria for the onset of a positive eigenvalue of the linearised system of equations (45), which we propose indicates the onset of a linear instability to shear banding as the underlying homogeneous base state evolves in time. However, as noted above, the concept of a time-dependent eigenvalue should be treated with some caution. Therefore in the right hand panel of Fig. 15 we show results obtained by integrating the linearised equations (45) directly. The solid lines are contours of equal $|\delta\dot{\gamma}_{n=1}|$, obtained by this process of integration. As can

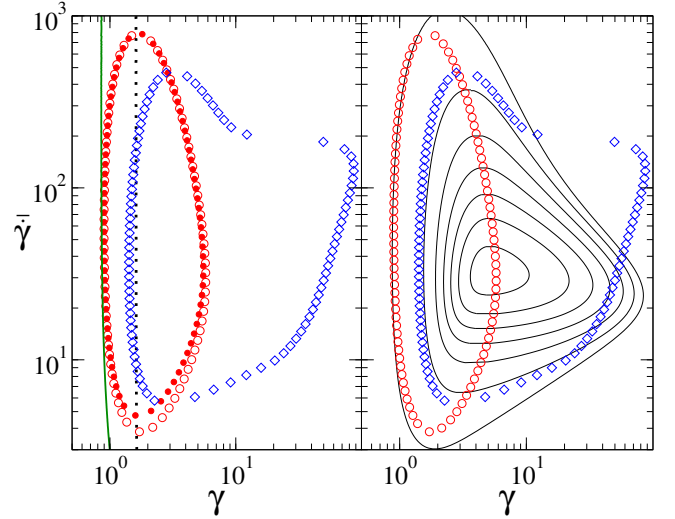


FIG. 16. As in Fig. 15 but now for nRP model with a monotonic constitutive curve, $\beta = 1.0$. The ‘viscous instability’ is absent in this case, but the ‘elastic instability’ remains.

be seen the region of growth and decay in this heterogeneous perturbation agrees well with the eigenvalue-based criteria in the left subpanel, confirming that our concept of a time-dependent eigenvalue is indeed useful.

We also summarise in Fig. 15 the results of a series of fully nonlinear spatially-aware simulations of shear startup, performed for a wide range of values of $\dot{\gamma}$ at closely spaced intervals. Again, any horizontal slice across this plane corresponds to one of these runs at a given $\dot{\gamma}_0$. The diamonds show the region of this plane of strain-rate and strain for which significant shear banding is observed. (We choose $\Delta_{\dot{\gamma}} > 0.05\dot{\gamma}$ as a criterion for significant banding.) As can be seen, the region of significant banding agrees well with expectations based on the linear calculation alone in most regions of the plane. However a window of shear rates either side of the regime of viscous linear instability deserves further comment. Here the nonlinear simulations remain significantly banded in steady state, even though the linear system has returned to stability by then. For such shear rates, a state of homogeneous shear on the underlying constitutive curve is indeed linearly stable, but in fact only metastable: the true steady state is banded. Finally at very high shear rates *e.g.* $\dot{\gamma} = 600$, we observe shear bands that form transiently in startup, triggered by the ‘elastic’ instability, but that return to homogeneous flow in steady state.

In summary, the overall stability portrait of the nRP model with a nonmonotonic constitutive curve comprises, in this plane of strain-rate and strain, a vertical patch of ‘elastic instability’ at the left side of the plane, and a horizontal patch of ‘viscous instability’ at the right hand side. In between these limits there is a continuous cross-over between the two instabilities.

In contrast, for model parameters for which the con-

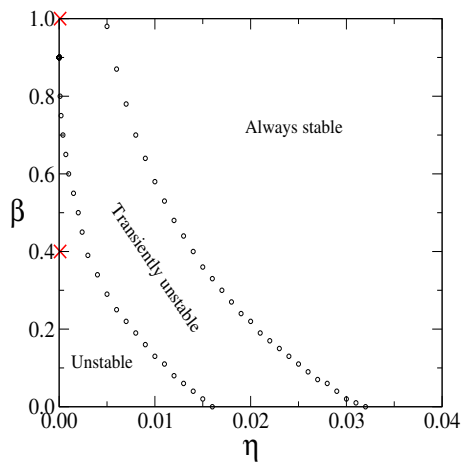


FIG. 17. Summary of the linear stability properties of the nRP model as a function of the model parameters β, η , during shear startup at a shear rate in the region of minimum slope of the constitutive curve. ‘*Unstable*’: linearly unstable to shear heterogeneity at steady state. ‘*Transiently unstable*’: system shows linear instability at some time during shear startup but returns to linearly stable at steady state. ‘*Always stable*’: the system is always linearly stable to shear heterogeneity. Crosses ‘ \times ’ at: $\beta = 1, 0.4$ at $\eta = 10^{-4}$ indicate the two sets of parameter values explored in detail in the text.

stitutive curve is monotonic, the patch of ‘viscous instability’ is absent and the eventual steady flowing state is homogeneous at all strain rates. Importantly, however, a patch of ‘elastic instability’ remains with onset at a strain $\gamma \approx 1$, again closely associated with the startup stress overshoot at strain $\gamma \approx 1.7$. See Fig. 16. This triggers pronounced shear banding during startup, which however persists only transiently, decaying at larger strains to leave homogeneous flow in steady state. A single startup run corresponding to a horizontal slice across this plane at $\dot{\gamma}_0 = 30.0$ is explored in 14 (top row). In steady state, the flow is homogeneous with a stress value indicated by the upper cross in Fig. 13.

So far, we have explored in detail one set of model parameters $(\beta, \eta) = (0.4, 10^{-4})$ for which the underlying constitutive curve is non-monotonic and a viscous instability persists to steady state; and one set of parameters $(\beta, \eta) = (1.0, 10^{-4})$ for which the constitutive curve is monotonic and shear bands form only transiently. Denoting these two distinct cases by “unstable” and “transiently unstable” respectively, we summarise the model’s behaviour in the full plane of (β, η) in Fig. 17.

2. Stretching RP model

In the previous subsection we discussed the predictions of the non-stretch rolie-poly (nRP) model, in which any possibility of chain stretch is switched off by setting $\tau_R = 0$. Recall Eqns. 11. We now turn to the sRP model in which chain stretch is accounted for. Recall Eqns. 10.

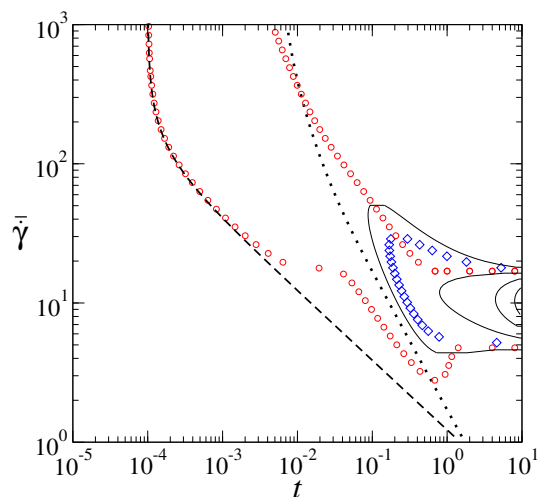


FIG. 18. Stability portrait of the sRP model in the plane of strain-rate and strain for model parameter values $\beta = 0.4$, $\eta = 10^{-4}$, $\tau_R = 10^{-2}$, $g = 5 \times 10^{-3}$. Solid lines show contours of equal $|\delta\dot{\gamma}_m| = \dot{\gamma}10^M$ for integer M found by directly integrating the linearised Eqns. 45. (The contour nearest $\partial_t \Sigma = 0$ has $M = -2$, and we show only contours $M \geq -2$.) Diamonds show the region of significant banding in a full nonlinear spatially aware simulation. For shear rates in the non-stretching regime $\tau_d^{-1} \ll \dot{\gamma} \ll \tau_R^{-1}$ we recover the behaviour discussed previously in the nRP model. In contrast an ‘sRP-specific’ instability is seen in upper-left region of the plane with onset given by the formula in Eqn. 54, which is shown by a dashed line. However it does not precipitate significant banding.

For applied strain rates $\dot{\gamma} \ll \tau_R^{-1}$, no appreciable stretch arises even in the sRP model, and the nRP results discussed above apply directly. This can be seen in Fig. 18: the dynamics in the regime $\dot{\gamma} \ll \tau_R^{-1}$ is the same as discussed above for the nRP model.

The focus in this section is therefore on shear startup runs performed at shear rates $\dot{\gamma} > \tau_R^{-1}$, for which appreciable chain stretch does develop. Here the system exhibits an early-time ($t < \tau_R$) stress-strain behaviour corresponding to that of a linear elastic solid, with $\Sigma = G\gamma$. At longer times $t > \tau_R$ the relaxation of chain stretch leads to deviation from this linear relation and a stress signal that decreases with strain, after an overshoot. In contrast to the nRP model, in which stress overshoot occurs at a fixed value of the strain, in the stretching regime this overshoot now occurs at a fixed time $t \sim \tau_R$. Accordingly, the stress startup curve no longer converges to a limiting function of strain $\Sigma = \Sigma(\gamma)$ at high shear rates, and the concept of a purely ‘elastic instability’ no longer applies. As can be seen in Fig. 18 the onset of an elastic instability just before overshoot is apparent only in the non-stretch regime $\dot{\gamma} \ll \tau_R^{-1}$ explored previously in the nRP model, and breaks down for $\dot{\gamma} > \tau_R^{-1}$.

Surprisingly, however, we find a new linear instability, specific to the stretching regime $\dot{\gamma}_0 > \tau_R^{-1}$, that sets in at

a time *before* overshoot given by

$$t_s = \frac{3}{2\tau_d\dot{\gamma}_0^2} + \eta/G \quad \text{for } \dot{\gamma}_0 \gg \tau_R^{-1}. \quad (54)$$

However this instability disappears again even before the overshoot occurs and never leads to observable banding, so we pursue it no further here.

3. Rolie-poly model: relation to shear startup experiments

We have shown that the RP model shows rich time-dependent banding dynamics during shear startup in the nonstretching regime $\tau_d^{-1} \ll \dot{\gamma} \ll \tau_R^{-1}$. These results, together with those of Adams *et al.*³⁻⁵, demonstrate that the RP model captures the experimental phenomenology of entangled polymeric fluids in this shear startup protocol. We summarise this now, divided into three classes (i) - (iii) for convenience.

(i) For imposed shear rates in the negatively sloping regime of a non-monotonic underlying constitutive curve, we find shear banding that sets in around the time of an overshoot in the stress startup curve and is initially sufficiently violent as to lead to elastic recoil and negative local shear rates or velocities. It persists to steady state but with much smaller magnitude than around the time of overshoot. This is consistent with experimental observations in Refs.^{14,15,73,75,84}. (ii) For imposed shear rates some distance above the negatively sloping regime of a non-monotonic constitutive curve, we again find violent shear banding setting in around the time of stress overshoot during startup. However these bands persist only transiently, and decay to leave a homogeneous steady state. This is consistent with experimental observations in Refs.^{15,75}. (iii) For a monotonic constitutive curve we again see pronounced transient banding triggered by stress overshoot, which decays to leave a homogeneous steady state, as in experimental observations in Refs.^{15,41,75}.

The main new contribution of the present manuscript has been to place these observations in the context of our general analytical criterion for the onset of banding.

C. Numerical results: Giesekus model

We now discuss our numerical results for shear startup in the Giesekus model. Our aim is to address whether this model is capable of capturing the time-dependent shear banding behaviour observed experimentally in entangled polymers, summarised in (i) - (iii) above. To provide a fair comparison with the RP model, we choose values of the parameter α giving constitutive curves that are as closely comparable between the models as possible. Compare Fig. 19 with Fig. 14.

To explore class (i) behaviour, we consider the non-monotonic constitutive curve of Fig. 19 and perform a shear startup at a value of the shear rate represented

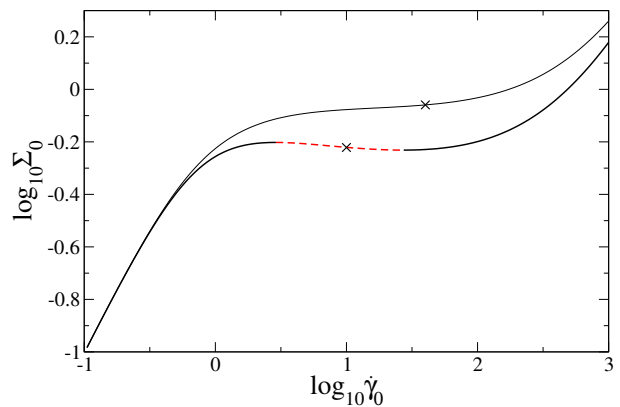


FIG. 19. Constitutive curves for the Giesekus model with $\alpha = 0.6, 0.8$ (top to bottom) and $\eta = 10^{-3}$. Regime of linear instability is shown as a dashed line. Crosses indicate shear rates $\dot{\gamma} = 10, 40$ for which time-dependent behaviour is shown in Figs. 20 and 21 respectively.

by the cross in the negatively sloping regime. See Fig. 20. The stress startup curve closely resembles that of the RP model, with a pronounced overshoot. However the Giesekus model apparently lacks the region of pronounced elastic instability associated with this overshoot. Instead, the degree of banding $\Delta_{\dot{\gamma}}$ rises monotonically and only becomes significant at long times, when the criterion $\partial_{\dot{\gamma}}\Sigma|_{\gamma \rightarrow \infty} < 0$ for viscous instability and steady state banding is met. For shear rates outside the negatively sloping regime of this constitutive curve (not shown), we find no banding during startup or in steady state. The Giesekus model therefore fails to address classes (i) and (ii) of polymeric startup behaviour described above.

To explore class (iii) behaviour, we consider the monotonic constitutive curve of Fig. 19 and perform a shear startup at a value of the shear rate represented by the cross in the region of weakest slope. See Fig. 21. The stress startup curve again closely resembles that of the RP model. However the magnitude of transient shear banding is significantly diminished in comparison, never exceeding 10% of the overall imposed shear rate $\bar{\dot{\gamma}}$. Indeed, no eigenvalue shows a positive real part during startup for a monotonic constitutive curve in this model. Accordingly, the Giesekus model lacks the pronounced ‘elastic instability’ of the RP model and fails to address class (iii) behaviour also.

A thorough exploration of this parameter space $\alpha, \eta, \bar{\dot{\gamma}}$ (not shown) confirms that the above comments of negligible banding during startup apply generically in the Giesekus model. This obviously contrasts sharply with our results for the RP model above. The reason for this appears to be the different structure of the loading terms between the Giesekus and RP models. Compare Eqns. 12 with Eqns. 11. Because of this difference, the Giesekus model does not attain a limiting nonlinear shear startup curve $\Sigma(\dot{\gamma})$ at high shear rates, and accordingly lacks the

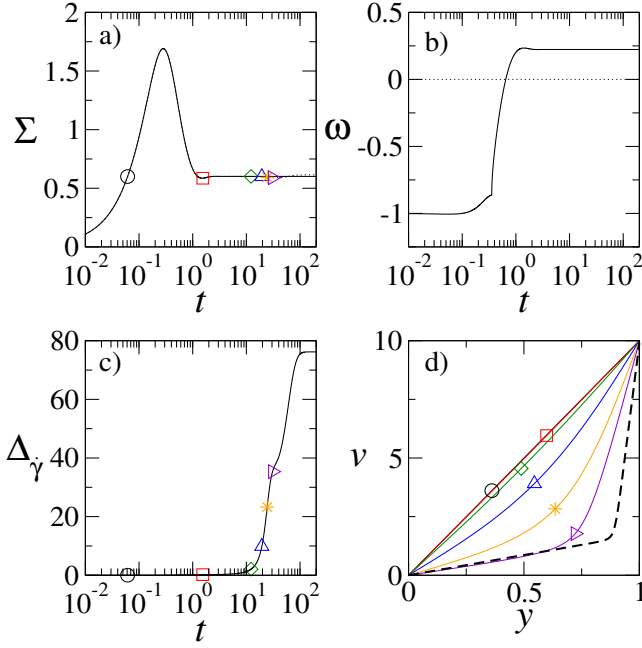


FIG. 20. Shear startup in Giesekus model at an applied shear rate $\bar{\gamma} = 10$ in the negative sloping regime of the non-monotonic constitutive curve of Fig. 19. (a) Shear stress startup curve (results with heterogeneity allowed are indistinguishable from the homogeneously constrained system). (b) Largest real part of any eigenvalue from linear stability analysis ω . (c) Degree of banding in the nonlinear simulation, $\Delta_{\dot{\gamma}} = \dot{\gamma}_{\max} - \dot{\gamma}_{\min}$. (d) Snapshots of the velocity profile in the nonlinear simulation at strains corresponding to symbols in (a, c). The steady state velocity profile is shown as a thick, dashed line. Magnitude of initial noise: $q = 10^{-2}$.

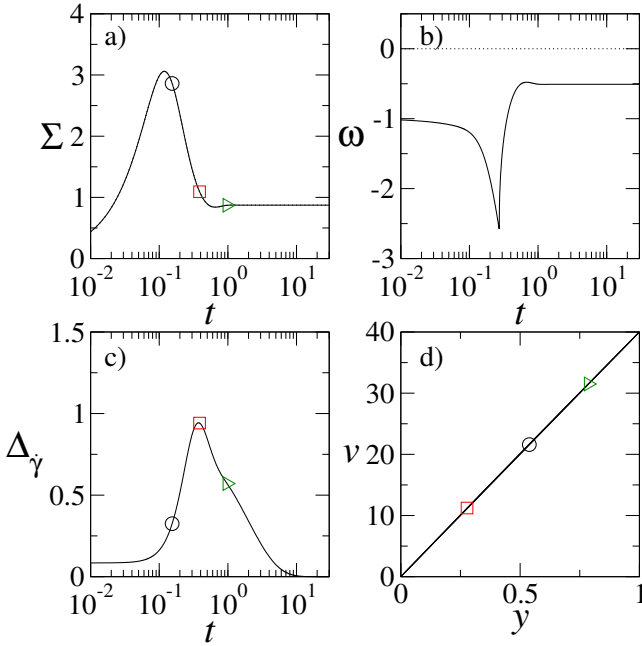


FIG. 21. As in Fig. 20, but now for an applied shear rate $\bar{\gamma} = 10$ at the weakest slope of the constitutive curve of Fig. 19 with $\alpha = 0.8$, $\eta = 10^{-3}$.

possibility of an elastic instability.

VIII. CONCLUSIONS AND OUTLOOK

We have explored theoretically the onset of shear banding in polymeric and wormlike micellar fluids for three of the most common time-dependent rheological protocols: step stress, strain ramp, and shear startup. For each protocol we have developed a fluid-universal criterion for the onset of linear instability to shear banding. We have supported these predictions with numerical simulations of the rolie-poly and Giesekus models. Between these models, we have found the rolie-poly model to be effective in capturing the observed experimental phenomenology. In contrast, the Giesekus model apparently fails to do so.

Following the imposition of a step stress, a base state of initially homogeneous creep response becomes unstable to the formation of shear bands during any regime in which the shear rate $\dot{\gamma}(t)$ is simultaneously upwardly curving and upwardly sloping in time $\partial_t^2 \dot{\gamma} / \partial_t \dot{\gamma} > 0$. We believe this criterion to be universal in all models for the rheology of complex fluids of which we are aware. We showed that such a regime does indeed arise in both the Giesekus and RP models for imposed stresses nearest those on the weakest slope of the underlying constitutive curve of shear stress as a function of shear rate. However the magnitude of the resulting shear banding only attains a magnitude consistent with experimental findings^{12,14,39,40,73,83} in the RP model.

For the strain ramp protocol, a base state of initially homogeneous shear response is left unstable immediately post-ramp if the stress had been decreasing with strain towards the end of the ramp. We believe this criterion to be general for all ramps applied at a rate exceeding the inverse of the material's intrinsic relaxation time, for any viscoelastic constitutive equation that can be expressed as the sum of separate loading and relaxation terms.

In the RP model, we demonstrated numerically that this criterion for instability immediately post-ramp is met for ramp rates in the nonstretching regime $\tau_d^{-1} \ll \dot{\gamma}_0 \ll \tau_R^{-1}$, and ramp amplitudes $\gamma_0 \gtrsim 1.7$. However we further explored the RP model's full relaxation as a function of the time elapsed since the ramp ended, following ramps that are either slow or fast relative to the rate of chain stretch relaxation τ_R^{-1} . In the absence of convective constraint release (CCR), the stress relaxation function of a 'fast' ramp drops onto that of a 'slow' ramp once chain stretch has relaxed. This leads to a delayed shear banding instability following a 'fast' ramp, even though in that case the stress increased monotonically with strain during the ramp. In contrast CCR tends to stabilise the system against this 'delayed' banding instability. In capturing such rich phenomenology, we again find the RP model capable of addressing the experimental data for polymeric fluids, while the Giesekus model would be expected to perform poorly in comparison.

Finally we explored the onset of shear banding in the shear startup protocol. For materials that attain a limiting nonlinear startup curve of stress as a function of strain at high strain rates, we identified separate ‘elastic’ and ‘viscous’ instabilities that respectively act at early and late times during startup. We confirmed the presence of these two distinct regimes in a numerical study of the RP model, which shows a violent elastic instability at early times during startup at rates $\tau_d^{-1} \ll \dot{\gamma} \ll \tau_R^{-1}$, closely associated with an overshoot in the stress startup signal. This banding persists to steady state in any regime of negative slope in the underlying constitutive curve (*i.e.* of viscous instability), but with a ‘degree of banding’ that is much weaker than that seen during the initial elastic instability. In contrast the Giesekus model does not attain a limiting startup curve of stress as a function of strain at high strain rates and lacks a violent elastic instability during startup, in contrast to experimental observations. It does, however, correctly capture steady state banding. Accordingly we conclude that the RP model provides a good description of shear banding during time-dependent flows in entangled polymeric fluids, while the Giesekus model performs poorly in comparison.

The reader is referred to a separate manuscript in which the fluid-universal criteria that we have derived here (and discussed in detail in the context of polymer fluids) are explored in the context of a broad class of disordered soft glassy materials including foams, dense emulsions and colloids³⁰.

IX. ACKNOWLEDGEMENTS

The authors thank Stephen Agimelen, Peter Olmsted, and Richard Graham for helpful discussions, and the UK’s EPSRC (EP/E5336X/1) for funding.

¹We note that, within the linear regime, the degree of banding $\Delta\dot{\gamma}$ scales linearly with the magnitude of the initial noise q . Therefore, in order to make comparisons with the RP model the results presented in sections V B and V C section have $q = 0.1$. We note that q values much larger than this are unrealistic for comparison to experiment.

²J. Adams, S. Fielding, and P. Olmsted. The interplay between boundary conditions and flow geometries in shear banding: Hysteresis, band configurations, and surface transitions. *Journal of Non-Newtonian Fluid Mechanics*, 151:101 – 118, 2008.

³J. M. Adams, S. M. Fielding, and P. D. Olmsted. Transient shear banding in entangled polymers: A study using the rolipoly model. *Journal of Rheology*, 55(5):1007–1032, 2011.

⁴J. M. Adams and P. D. Olmsted. Adams and olmsted reply. *Phys. Rev. Lett.*, 103:219802, 2009.

⁵J. M. Adams and P. D. Olmsted. Nonmonotonic models are not necessary to obtain shear banding phenomena in entangled polymer solutions. *Phys. Rev. Lett.*, 102:067801, 2009.

⁶O. S. Agimelen. *TBC*. PhD thesis, University of Leeds, 2012.

⁷O. S. Agimelen and P. D. Olmsted. Apparent fracture in polymeric fluids under step shear. *Phys. Rev. Lett.*, 110:204503, 2013.

⁸L. A. Archer. Separability criteria for entangled polymer liquids. *Journal of Rheology*, 43(6):1555–1571, 1999.

⁹L. A. Archer, Y.-L. Chen, and R. G. Larson. Delayed slip after step strains in highly entangled polystyrene solutions. *Journal of Rheology*, 39(3):519–525, 1995.

¹⁰J. Azaiez, R. Gunette, and A. Ait-Kadi. Entry flow calculations using multi-mode models. *Journal of Non-Newtonian Fluid Mechanics*, 66(2-3):271 – 281, 1996.

¹¹J.-F. Berret and Y. S  r  ro. Evidence of shear-induced fluid fracture in telechelic polymer networks. *Phys. Rev. Lett.*, 87:048303, 2001.

¹²P. E. Boukany and S.-Q. Wang. Use of particle-tracking velocimetry and flow birefringence to study nonlinear flow behavior of entangled wormlike micellar solution: From wall slip, bulk disentanglement to chain scission. *Macromolecules*, 41(4):1455–1464, 2008.

¹³P. E. Boukany and S.-Q. Wang. Exploring origins of interfacial yielding and wall slip in entangled linear melts during shear or after shear cessation. *Macromolecules*, 42(6):2222–2228, 2009.

¹⁴P. E. Boukany and S.-Q. Wang. Exploring the transition from wall slip to bulk shearing banding in well-entangled dna solutions. *Soft Matter*, 5:780–789, 2009.

¹⁵P. E. Boukany and S.-Q. Wang. Shear banding or not in entangled DNA solutions depending on the level of entanglement. *Journal of Rheology*, 53(1):73–83, 2009.

¹⁶P. E. Boukany, S.-Q. Wang, and X. Wang. Step shear of entangled linear polymer melts: New experimental evidence for elastic yielding. *Macromolecules*, 42(16):6261–6269, 2009.

¹⁷S. R. Burdette. Development of the velocity field in transient shear flows of viscoelastic fluids. *Journal of Non-Newtonian Fluid Mechanics*, 32(3):269 – 294, 1989.

¹⁸J. A. Byars, R. J. Binnington, and D. V. Boger. Entry flow and constitutive modelling of fluid S1. *Journal of Non-Newtonian Fluid Mechanics*, 72(2-3):219 – 235, 1997.

¹⁹J. Cao and A. E. Likhtman. Shear banding in molecular dynamics of polymer melts. *Phys. Rev. Lett.*, 108:028302, 2012.

²⁰M. E. Cates. Nonlinear viscoelasticity of wormlike micelles (and other reversibly breakable polymers). *The Journal of Physical Chemistry*, 94(1):371–375, 1990.

²¹P. Coussot, J. S. Raynaud, F. Bertrand, P. Moucheront, J. P. Guilbaud, H. T. Huynh, S. Jarny, and D. Lesueur. Coexistence of liquid and solid phases in flowing soft-glassy materials. *Phys. Rev. Lett.*, 88:218301, 2002.

²²T. Divoux, C. Barentin, and S. Manneville. From stress-induced fluidization processes to Herschel-Bulkley behaviour in simple yield stress fluids. *Soft Matter*, 7:8409–8418, 2011.

²³T. Divoux, C. Barentin, and S. Manneville. Stress overshoot in a simple yield stress fluid: An extensive study combining rheology and velocimetry. *Soft Matter*, 7:9335–9349, 2011.

²⁴T. Divoux, D. Tamarii, C. Barentin, and S. Manneville. Transient shear banding in a simple yield stress fluid. *Phys. Rev. Lett.*, 104:208301, 2010.

²⁵M. Doi and S. F. Edwards. Dynamics of concentrated polymer systems. Part 2 Molecular motion under flow. *J. Chem. Soc., Faraday Trans. 2*, 74:1802–1817, 1978.

²⁶M. Doi and S. F. Edwards. *The Theory of Polymer Dynamics*. Clarendon, Oxford, 1989.

²⁷Y. Einaga, K. Osaki, M. Kurata, S. Kimura, and M. Tamura. Stress relaxation of polymer solutions under large strain. *Polymer Journal*, 2(4):550–552, 1971.

²⁸Y. Fang, G. Wang, N. Tian, X. Wang, X. Zhu, P. Lin, G. Ma, and L. Li. Shear inhomogeneity in poly(ethylene oxide) melts. *Journal of Rheology*, 55(5):939–949, 2011.

²⁹S. M. Fielding. Complex dynamics of shear banded flows. *Soft Matter*, 3:1262–1279, 2007.

³⁰S. M. Fielding. Shear banding in soft glassy materials, in preparation. 2013.

³¹S. M. Fielding and P. D. Olmsted. Kinetics of the shear banding instability in startup flows. *Phys. Rev. E*, 68:036313, 2003.

³²T. Gibaud, D. Frelat, and S. Manneville. Heterogeneous yielding dynamics in a colloidal gel. *Soft Matter*, 6:3482–3488, 2010.

- ³³H. Giesekus. A simple constitutive equation for polymer fluids based on the concept of deformation-dependent tensorial mobility. *Journal of Non-Newtonian Fluid Mechanics*, 11(12):69–109, 1982.
- ³⁴R. S. Graham, A. E. Likhtman, T. C. B. McLeish, and S. T. Milner. Microscopic theory of linear, entangled polymer chains under rapid deformation including chain stretch and convective constraint release. *Journal of Rheology*, 47(5):1171–1200, 2003.
- ³⁵P. Hebraud, F. Lequeux, P. Sollich, and M. E. Cates. *Physical Review Letters*, 78:2020–2023, 1997.
- ³⁶M. E. Helgeson, M. D. Reichert, Y. T. Hu, and N. J. Wagner. Relating shear banding, structure, and phase behavior in wormlike micellar solutions. *Soft Matter*, 5:3858–3869, 2009.
- ³⁷M. E. Helgeson, P. A. Vasquez, E. W. Kaler, and N. J. Wagner. Rheology and spatially resolved structure of cetyltrimethylammonium bromide wormlike micelles through the shear banding transition. *Journal of Rheology*, 53(3):727–756, 2009.
- ³⁸Y. T. Hu. Steady-state shear banding in entangled polymers? *Journal of Rheology*, 54(6):1307–1323, 2010.
- ³⁹Y. T. Hu and A. Lips. Kinetics and mechanism of shear banding in an entangled micellar solution. *Journal of Rheology*, 49(5):1001–1027, 2005.
- ⁴⁰Y. T. Hu, C. Palla, and A. Lips. Comparison between shear banding and shear thinning in entangled micellar solutions. *Journal of Rheology*, 52(2):379–400, 2008.
- ⁴¹Y. T. Hu, L. Wilen, A. Philips, and A. Lips. Is the constitutive relation for entangled polymers monotonic? *Journal of Rheology*, 51(2):275–295, 2007.
- ⁴²Y. W. Inn, K. F. Wissbrun, and M. M. Denn. Effect of edge fracture on constant torque rheometry of entangled polymer solutions. *Macromolecules*, 38(22):9385–9388, 2005.
- ⁴³M. T. Islam, J. Sanchez-Reyes, and L. A. Archer. Nonlinear rheology of highly entangled polymer liquids: Step shear damping function. *Journal of Rheology*, 45(1):61–82, 2001.
- ⁴⁴Juliani and L. A. Archer. Linear and nonlinear rheology of bidisperse polymer blends. *Journal of Rheology*, 45(3):691–708, 2001.
- ⁴⁵S. A. Khan and R. G. Larson. Comparison of simple constitutive equations for polymer melts in shear and biaxial and uniaxial extensions. *Journal of Rheology*, 31(3):207–234, 1987.
- ⁴⁶R. Larson. *Constitutive Equations for Polymer Melts and Solutions*. Butterworth Publishers, Stoneham, MA, 1988.
- ⁴⁷R. G. Larson. *The Structure and Rheology of Complex Fluids*. Oxford University Press Inc., New York, 1999.
- ⁴⁸S. Lerouge and J.-F. Berret. Shear-induced transitions and instabilities in surfactant wormlike micelles. In K. Dusek and J.-F. Joanny, editors, *Polymer Characterization*, volume 230 of *Advances in Polymer Science*, pages 1–71. Springer Berlin Heidelberg, 2010.
- ⁴⁹X. Li and S.-Q. Wang. Elastic yielding after step shear and during laos in the absence of meniscus failure. *Rheologica Acta*, 49:985–991, 2010.
- ⁵⁰A. E. Likhtman and R. S. Graham. Simple constitutive equation for linear polymer melts derived from molecular theory: Rolie-poly equation. *Journal of Non-Newtonian Fluid Mechanics*, 114(1):1–12, 2003.
- ⁵¹C.-Y. D. Lu, P. D. Olmsted, and R. C. Ball. Effects of nonlocal stress on the determination of shear banding flow. *Phys. Rev. Lett.*, 84:642, 2000.
- ⁵²R. W. Mair and P. T. Callaghan. Observation of shear banding in worm-like micelles by NMR velocity imaging. *Europhysics Letters*, 36(9):719, 1996.
- ⁵³R. W. Mair and P. T. Callaghan. Shear flow of wormlike micelles in pipe and cylindrical couette geometries as studied by nuclear magnetic resonance microscopy. *Journal of Rheology*, 41(4):901–924, 1997.
- ⁵⁴R. Makhloufi, J. P. Decruppe, A. At-Ali, and R. Cressely. Rheo-optical study of worm-like micelles undergoing a shear banding flow. *Europhysics Letters*, 32(3):253, 1995.
- ⁵⁵S. Manneville. Recent experimental probes of shear banding. *Rheologica Acta*, 47:301–318, 2008.
- ⁵⁶S. Manneville, A. Colin, G. Waton, and F. Schosseler. Wall slip, shear banding, and instability in the flow of a triblock copolymer micellar solution. *Phys. Rev. E*, 75:061502, 2007.
- ⁵⁷M. L. Manning, J. S. Langer, and J. M. Carlson. Strain localization in a shear transformation zone model for amorphous solids. *Phys. Rev. E*, 76:056106, 2007.
- ⁵⁸G. Marrucci and N. Grizzuti. The free energy function of the Doi-Edwards theory: analysis of the instabilities in stress relaxation. *Journal of Rheology*, 27(5):433–450, 1983.
- ⁵⁹E. Miller and J. P. Rothstein. Transient evolution of shear-banding wormlike micellar solutions. *Journal of Non-Newtonian Fluid Mechanics*, 143(1):22–37, 2007.
- ⁶⁰R. L. Moorcroft, M. E. Cates, and S. M. Fielding. Age-dependent transient shear banding in soft glasses. *Phys. Rev. Lett.*, 106:055502, 2011.
- ⁶¹R. L. Moorcroft and S. M. Fielding. Criteria for shear banding in time-dependent flows of complex fluids. *Phys. Rev. Lett.*, 110:086001, 2013.
- ⁶²P. D. Olmsted. Perspectives on shear banding in complex fluids. *Rheologica Acta*, 47:283–300, 2008.
- ⁶³P. D. Olmsted, O. Radulescu, and C.-Y. D. Lu. Johnson–Segalman model with a diffusion term in cylindrical couette flow. *Journal of Rheology*, 44(2):257–275, 2000.
- ⁶⁴K. Osaki. On the damping function of shear relaxation modulus for entangled polymers. *Rheologica Acta*, 32:429–437, 1993.
- ⁶⁵K. Osaki and M. Kurata. Experimental appraisal of the Doi-Edwards theory for polymer rheology based on the data for polystyrene solutions. *Macromolecules*, 13(3):671–676, 1980.
- ⁶⁶K. Osaki, K. Nishizawa, and M. Kurata. Material time constant characterizing the nonlinear viscoelasticity of entangled polymeric systems. *Macromolecules*, 15(4):1068–1071, 1982.
- ⁶⁷K. Osaki and J. L. Schrag. Viscoelastic properties of polymer solutions in high-viscosity solvents and limiting high-frequency behavior. I. Polystyrene and Poly- α -methylstyrene. *Polymer Journal*, 2(4):541–549, 1971.
- ⁶⁸G. Ovarlez, S. Rodts, X. Chateau, and P. Coussot. Phenomenology and physical origin of shear localization and shear banding in complex fluids. *Rheologica Acta*, 48:831–844, 2009.
- ⁶⁹J. Paredes, N. Shahidzadeh-Bonn, and D. Bonn. Shear banding in thixotropic and normal emulsions. *Journal of Physics: Condensed Matter*, 23(28):284116, 2011.
- ⁷⁰W. H. Press, S. A. Teukolsky, W. T. Vetterling, and B. P. Flannery. *Numerical Recipes in C*. Cambridge University Press, Cambridge, 1992.
- ⁷¹L. M. Quinzani, G. H. McKinley, R. A. Brown, and R. C. Armstrong. Modeling the rheology of polyisobutylene solutions. *Journal of Rheology*, 34(5):705–748, 1990.
- ⁷²S. Ravindranath and S.-Q. Wang. What are the origins of stress relaxation behaviors in step shear of entangled polymer solutions? *Macromolecules*, 40(22):8031–8039, 2007.
- ⁷³S. Ravindranath and S.-Q. Wang. Steady state measurements in stress plateau region of entangled polymer solutions: Controlled-rate and controlled-stress modes. *Journal of Rheology*, 52(4):957–980, 2008.
- ⁷⁴S. Ravindranath, S.-Q. Wang, M. Olechnowicz, V. Chavan, and R. Quirk. How polymeric solvents control shear inhomogeneity in large deformations of entangled polymer mixtures. *Rheologica Acta*, 50:97–105, 2011.
- ⁷⁵S. Ravindranath, S.-Q. Wang, M. Olechnowicz, and R. P. Quirk. Banding in simple steady shear of entangled polymer solutions. *Macromolecules*, 41(7):2663–2670, 2008.
- ⁷⁶S. Rodts, J. C. Baudez, and P. Coussot. From ‘discrete’ to ‘continuum’ flow in foams. *Europhysics Letters*, 69(4):636, 2005.
- ⁷⁷S. A. Rogers, D. Vlassopoulos, and P. T. Callaghan. Aging, yielding, and shear banding in soft colloidal glasses. *Phys. Rev. Lett.*, 100:128304, 2008.
- ⁷⁸V. Rolón-Garrido and M. Wagner. The damping function in rheology. *Rheologica Acta*, 48:245–284, 2009.
- ⁷⁹J.-B. Salmon, A. Colin, S. Manneville, and F. Molino. Velocity profiles in shear-banding wormlike micelles. *Phys. Rev. Lett.*,

- 90:228303, 2003.
- ⁸⁰J.-B. Salmon, S. Manneville, and A. Colin. Shear banding in a lyotropic lamellar phase. I. Time-averaged velocity profiles. *Phys. Rev. E*, 68:051503, 2003.
- ⁸¹J. Sanchez-Reyes and L. A. Archer. Step shear dynamics of entangled polymer liquids. *Macromolecules*, 35(13):5194–5202, 2002.
- ⁸²P. J. Schmid. Nonmodal stability theory. *Annual Review of Fluid Mechanics*, 39(1):129–162, 2007.
- ⁸³P. Tapadia and S.-Q. Wang. Yieldlike constitutive transition in shear flow of entangled polymeric fluids. *Phys. Rev. Lett.*, 91:198301, 2003.
- ⁸⁴P. Tapadia and S.-Q. Wang. Direct visualization of continuous simple shear in non-newtonian polymeric fluids. *Phys. Rev. Lett.*, 96:016001, 2006.
- ⁸⁵D. C. Venerus. A critical evaluation of step strain flows of entangled linear polymer liquids. *Journal of Rheology*, 49(1):277–295, 2005.
- ⁸⁶C. M. Vrentas and W. W. Graessley. Study of shear stress relaxation in well-characterized polymer liquids. *Journal of Rheology*, 26(4):359–371, 1982.
- ⁸⁷J. M. W. and S. J. *Journal of Non-Newtonian Fluid Mechanics*, 2:255–270, 1977.
- ⁸⁸S.-Q. Wang, S. Ravindranath, P. Boukany, M. Olechnowicz, R. P. Quirk, A. Halasa, and J. Mays. Nonquiescent relaxation in entangled polymer liquids after step shear. *Phys. Rev. Lett.*, 97:187801, 2006.
- ⁸⁹J. Yerushalmi, S. Katz, and R. Shinnar. The stability of steady shear flows of some viscoelastic fluids. *Chemical Engineering Science*, 25(12):1891 – 1902, 1970.
- ⁹⁰L. Zhou, P. A. Vasquez, L. P. Cook, and G. H. McKinley. Modeling the inhomogeneous response and formation of shear bands in steady and transient flows of entangled liquids. *Journal of Rheology*, 52(2):591–623, 2008.